Technical report to spin polarizabilities of the proton by measurement of Compton double-polarization observables

D. Paudyal[*] and G.M. Huber
University of Regina, Regina, Saskatchewan S4S 0A2, Canada

P.P. Martel
Mount Allison University, Sackville, New Brunswick E4L 1E6, Canada and
Institut für Kernphysik, University of Mainz, 55128 Mainz, Germany

D. Hornidge
Mount Allison University, Sackville, New Brunswick E4L 1E6, Canada
(Dated: February 12, 2019)

This report outlines technical support of the manuscript on "Spin polarizabilities of the proton via measurement of Compton double-polarization observables" that was submitted to the A2 collaboration for internal review. It also presents π^0 photoproduction $\sum_{2z}$ asymmetry results from polarized Compton scattering performed at the Mainz Microtron. The experiments were run during two periods, May 2014 and June/July 2015, using a circularly polarized photon beam incident on a longitudinally polarized, frozen spin butanol target. In addition, this report summarizes various corrections that are vital for $\sum_{2z}$ Compton scattering asymmetry studies including carbon and helium scaling factors, and target polarization studies.

I. INTRODUCTION

Proton Compton scattering, $\gamma p \to \gamma p$, is only one of the many interactions that can occur when photons hit a nuclear target. Although Compton scattering seems to have a simple final state, it is very important to correctly identify the individual particles detected in the Crystal Ball (CB) and Two Arms Photon Spectrometer (TAPS) detector system. The background from other competing reactions has to be identified and suppressed with several analyses of the reaction kinematics. The biggest challenge is to properly understand the π^0 photoproduction background because its cross section is about one hundred times larger than that of Compton scattering. Therefore, exclusive π^0 photoproduction is not only a significant source of "physics background" to Compton scattering experiments, but also a useful reaction for systematic tests of experimental systems and methodology of the analysis.

This report provides an overview of the π^0 photo production asymmetry and checks on various corrections applied to Compton $\sum_{2z}$ asymmetry studies. It should be pointed out that the manuscript on "Spin polarizabilities of the proton via measurement of Compton double-polarization observables" was submitted to the A2 collaboration for internal review and reviewers provided their comments. In addition, this report provides the cross-check on extra target polarization correction factors reported by the Bonn group due to an extra layer

———

* paudyald@uregina.ca

of ice on the outer Nuclear Magnetic Resonance (NMR) coil in all of the data runs taken from May 2013 to October 2015 [1]. This was done by including the simulation of coherent π^0 production on ^{4}He (Sec. III C 3), and from helicity dependent cross section studies (Sec. V).

II. $\pi^0 \sum_{2z}$ ASYMMETRY

The π^0 photo production asymmetry $\sum_{2z}$ can be expressed in terms of the polarized cross section with a flip in the polarization direction as:

$$\sum_{2z} = \frac{1}{P_{circ}^{\gamma} \cdot P_z^t} \left[\frac{(\sigma_{+z}^R + \sigma_{-z}^L) - (\sigma_{+z}^L + \sigma_{-z}^R)}{(\sigma_{+z}^R + \sigma_{-z}^L) + (\sigma_{+z}^L + \sigma_{-z}^R)} \right], \quad (1)$$

where $\sigma_{\pm z}^R$ and $\sigma_{\pm z}^L$ represent the cross section for right-handed and left-handed helicity states of the beam with the target polarized in $\pm z$ direction, and P_{circ}^{γ} and P_z^t are the degrees of the photon beam circular polarization and longitudinal target polarization, respectively. This can be simply visualized from the four beam-target orientations as shown in Figs. 1a – 1d.

The benefit of calculating an asymmetry is that the absolute normalizations (target density, beam flux, tagging and detection efficiencies) that relate the cross section to the number of events, N, cancel in the ratio. Therefore, the asymmetry formula in terms of count rate can be written as follows:

$$\sum_{2z} = \frac{1}{P_{circ}^{\gamma} \cdot P_z^t} \left[\frac{(N_{+z}^R + N_{-z}^L) - (N_{+z}^L + N_{-z}^R)}{(N_{+z}^R + N_{-z}^L) + (N_{+z}^L + N_{-z}^R)} \right], \quad (2)$$
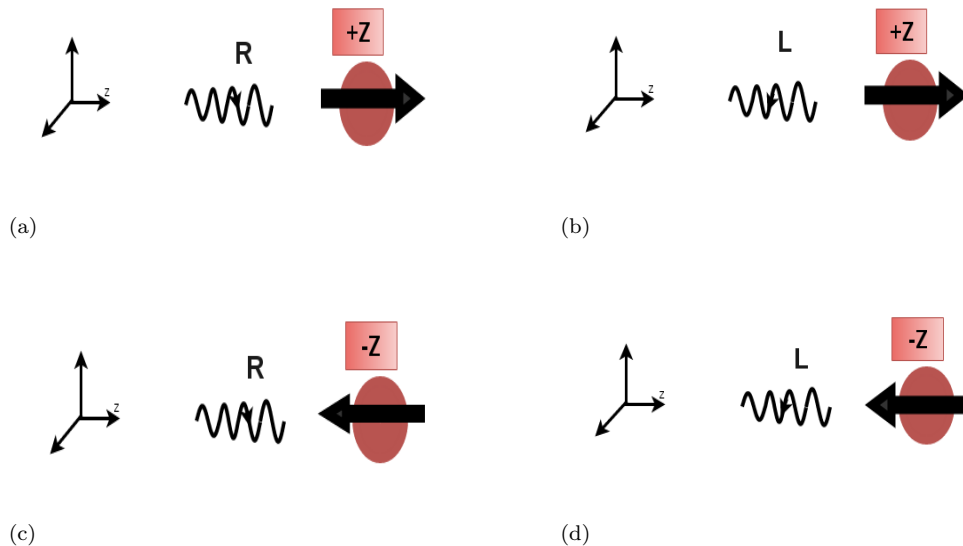
FIG. 1: Different orientations for π^0 photo production with a circularly polarized photon beam on a longitudinally polarized target. (a), (b) show the right and left helicity state of the beam with target polarization in $+z$ direction (σ_{+z}^R, σ_{+z}^L). (c) and (d) show the right and left helicity state of the beam with target polarization in $-z$ direction (σ_{-z}^R, σ_{-z}^L).

where $N_{\pm z}^R$ and $N_{\pm z}^L$ are the normalized yield for right and left helicity states of the beam with the target polarized in $\pm z$ direction.

III. BASIC ANALYSIS STEPS

In this section, the data analysis steps for the $\gamma p \rightarrow p\pi^0$ reaction channel, identification and reconstruction of particles (photons and protons) directly observed in the CB-TAPS detector system, the reconstruction of the π^0 from its decay, $\pi^0 \rightarrow \gamma\gamma$, and the various kinematic cuts applied are presented.

A. Particle Identification

To identify the particles of interest for the reaction channel, $\gamma p \rightarrow \pi^0 p$, with the π^0 decaying into two photons ($\pi^0 \rightarrow \gamma\gamma$), individual particle tracks were identified. The experimental setup, combining the CB and TAPS detectors with additional detector elements for charged particle identification and tracking was identical to the one used for the results reported in [2]. The Particle Identification Detector (PID) is a cylindrical detector consisting of 24 plastic scintillators parallel to the beam axis sorrounded by Multi-Wire Proportional Chambers (MWPCs). It is mounted around the target cell. By matching a hit in the PID with a corresponding hit in the CB, it is possible to use the $\Delta E/E$ technique to identify the charged particle species. In this technique, a coincident deposited energy in the PID versus the cluster energy in CB is used for the separation of charged pions, electrons, and protons. As for the lighter particles, like electrons and pions, the energy deposition is roughly $1-2$ MeV. However, heavier particles like the proton deposit energy inversely proportional to their total energy, with slower protons depositing a higher fraction of their total energy. A two-dimensional histogram of the energy loss, ΔE, measured in the PID, and the energy, E, measured in the CB, results in two distinct bands associated with different particle species. In addition, the MWPCs were used to track a charged particle track. In the case of TAPS, the veto detector tiles in front of each BaF$_2$ crystals are used. A cluster is identified as a charged particle if the veto tile in front of the cluster's central crystal is hit, and a cut placed on the cluster size separates the photons and neutrons (details can be found in [2]).

For an inclusive reaction channel, $\gamma p \rightarrow \pi^0 p$, the π^0 is identified through particle reconstruction. In addition to π^0 photoproduction, a single charged particle track is allowed but explicit detection of it is not required. This charged particle track is be assumed to be the recoil proton. In this case, the separation of charged particle track and neutrals is sufficient. It should be pointed out that any NaI and BaF$_2$ hits that are not identified as charged particles are processed as neutrals. The data

analysis was completed for single π^0 photoproduction and single π^0 plus a recoil proton in final state, but the difference in particle yield and asymmetry results was minimal: less than 1%. Therefore, the details of the distinction between protons, charged pions, and electrons have almost no impact at lower energies. In this report, only those particles produced from two photons are considered for the data analysis.

B. π^0 Reconstruction

The analysis of the reaction channel $\gamma p \rightarrow \pi^0 p$ requires events with exactly two time-correlated neutral particles in CB-TAPS that participate in a reaction with the target. This is due to the fact that some photons from the beam pass through without interacting, while many others are lost due to collimation of the beam. The events in the tagger that are in timing coincidence with the photons interacting with the target are called "prompt" events while those without any timing coincidences are "random" events. These uncorrelated events, which are normally referred to as background events, are numerous and hence need to be subtracted during the analysis.
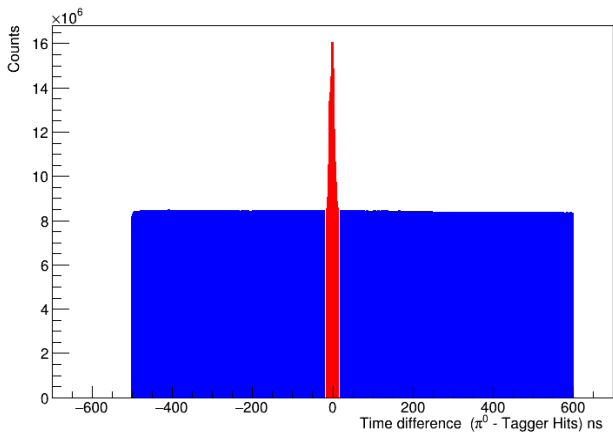

FIG. 2: Difference between the tagger and π^0 times; the prompt and random windows are shown in red and blue, respectively.

Fig. 2 shows the prompt and random timing windows for event hits in the tagger, which are in timing coincidence with the reconstructed π^0. The prompt electrons have a peak around 0 ns (shown in red) for detector element hits corresponding to photons that interacted with the target and the random electrons on either side of the prompt peak (blue background). The timing coincidence window of 30 ns is used to identify prompt electrons. The prompt peak sits on the top of a flat background associated with random electrons; therefore

a random coincidence subtraction was performed based on the weighted events of the random window on either side of prompt peak.

The energy and momentum information of two decay photons is used to reconstruct π^0 mesons. The invariant mass of the π^0 is defined as

$$M_{\gamma\gamma} = \sqrt{E_{\gamma\gamma}^2 - \vec{p}_{\gamma\gamma}^2} = \sqrt{(E_{\gamma_1} + E_{\gamma_2})^2 - (\vec{p}_{\gamma_1} + \vec{p}_{\gamma_2})^2}, \tag{3}$$

where E_{γ_1}, E_{γ_2}, $\vec{p}_{\gamma_1}$ and $\vec{p}_{\gamma_2}$ are the energy and the momentum vectors of the two photons, respectively. The π^0 reconstruction is performed to identify particles belonging only to its decay. A photon pair resulting from a π^0 decay should have an invariant mass of 134.98 MeV/c^2 within experimental resolution. An invariant mass width, $w_{\pi^0} = \pm17.5$ MeV/c^2, was applied, as shown in Fig. 3.
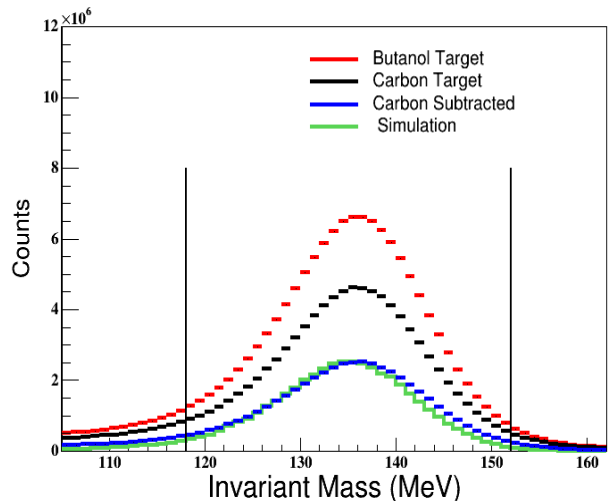

FIG. 3: An example invariant mass distribution (red: butanol target, black: carbon target, blue: carbon subtracted and green: simulation) for reconstructed π^0 photoproduction events at tagged photon energy, $E_\gamma = 285 - 305$ MeV. The two black vertical lines show a cut applied on the weighted invariant mass.

C. Carbon Background and checks on scaling factors

In this section, additional corrections and checks for consistency that have not been covered in D. Paudyal's thesis [2] are described. It should be pointed out that the four-fold method of subtraction (see Sec. II) was applied in this data analysis compared to the two-fold method as carried out in [2].

1. Base Scaling Factor

The $\sum_{2z}$ asymmetry experimental runs were broken down into two main parallel and anti-parallel data sets as well as subsets for positive and negative butanol target polarization runs for both the 2014 and 2015 beamtimes. Apart from the butanol target, separate dedicated data sets were taken with the carbon target after the butanol beamtimes. These carbon data that are also known as background data were analyzed using the same A2 GoAT physics class [3], followed by the user physics class as the butanol data. This was required to remove any contribution from the non-hydrogen elements in the butanol target. While the target is not a pure proton target, the unpolarized background from 'heavy' nuclei such as carbon and oxygen present in the butanol target can be partly removed by kinematic studies. There are several kinematic variables that play an important role in subtracting out the carbon contribution to the missing mass spectra. Two such variables playing an important role in subtracting out the carbon contribution to the missing mass spectra are the photon beam polarization and the carbon scaling factor. The scaling factor scales the separate experimental runs on a carbon target to each of the runs on the polarized butanol target.
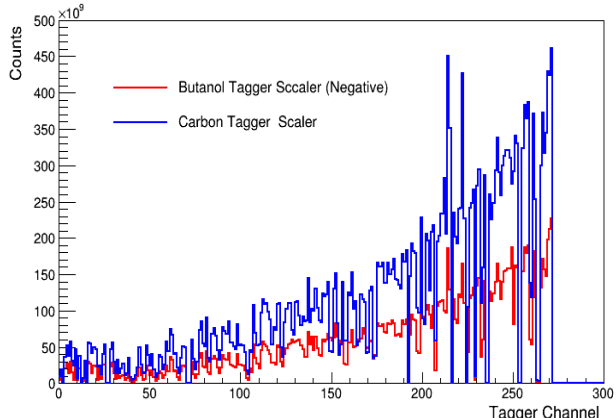

FIG. 4: An example tagger scaler distribution for negatively polarized butanol target and carbon target from the 2014 beamtime.

In order to scale the carbon data set, the ratio of the overall butanol target integrated luminosity to the overall carbon target integrated luminosity was determined, and this was termed the "base scaling factor". This was done by adding live-time corrected individual tagger scaler histograms for the entire data set (one for positive, one for negative target polarization, and one for the carbon background target) and dividing the butanol by the carbon data subset. The base scaling factor
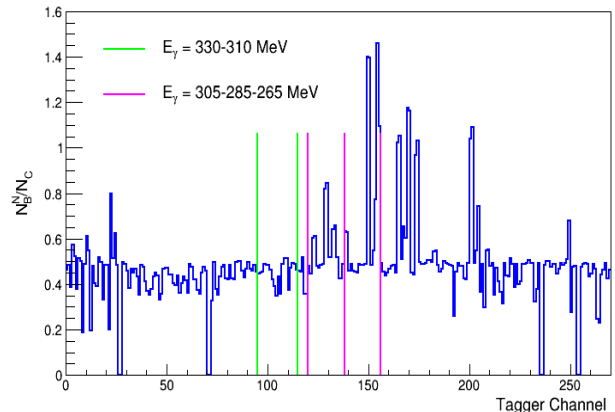

FIG. 5: Ratio of negatively polarized butanol target to carbon tagger scalers from the 2014 beamtime. The vertical lines show the tagged energy range of interest corresponding to tagger channels. The The fluctuations represent missing tagger channels not the statistical fluctuations.

is different for different subsets, as well as for different regions of the tagger. An example distribution of negatively polarized butanol (blue) and carbon target total histograms (red) from the 2014 beamtime are shown in Fig. 4 and the ratio between them for each tagger channel is shown in Fig. 5. Similarly, the positively polarized butanol (blue) and carbon target total histograms (red) and the ratio between them corresponding to each tagger channel are shown in Appendix B (Fig. 39a and Fig. 39b).

2. Determination of extra Carbon scaling factor

The base carbon scaling factor was obtained from a ratio of tagger scalers. However, this was insufficient to account for the nuclear π^0 photoproduction background due to additional nuclear effects and hence the missing mass ratio method was used to find the extra correction needed to properly scale the carbon runs. For this, missing mass spectra for the carbon target were scaled by the base scaling factor and then the missing mass spectra obtained with the butanol target were divided by the missing mass spectra obtained with the carbon target for the π^0 photoproduction channel. A combination of a Gaussian and a constant was fitted to the resulting spectra. The magnitude of the constant fitting parameter (Fig. 6) was used as an extra scaling factor. This was done separately for all four beam-target orientations and eighteen angular bins (see Appendix B), and an example plot is as shown in Fig. 7. The source of the systematic error arose mainly from the choice of

fitting range. The fitting range was varied from ± 40 MeV from the mean position of the spectrum and the average deviation of the π^0 photoproduction was used to determine the systematic uncertainty [2].
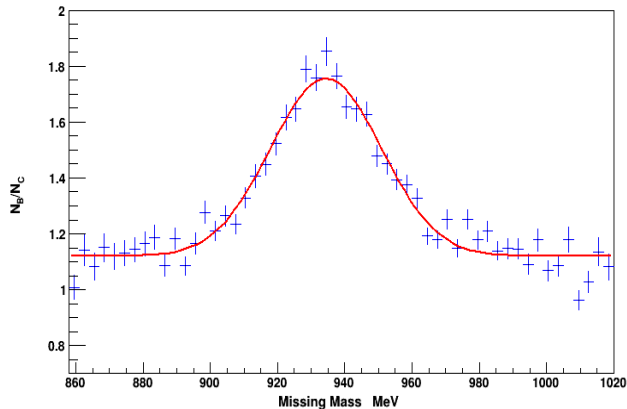

FIG. 6: An example spectrum of the ratio of missing proton mass for butanol and carbon targets in the energy range $E_\gamma = 285 - 305$ MeV at photon angle, $\theta = 110 - 120°$, for P0C0 (see Appendix A for nomenclature details) dataset. The red line is the combined fit of a Gaussian plus a constant term. The fit parameter of the constant defines the extra carbon scaling factor.
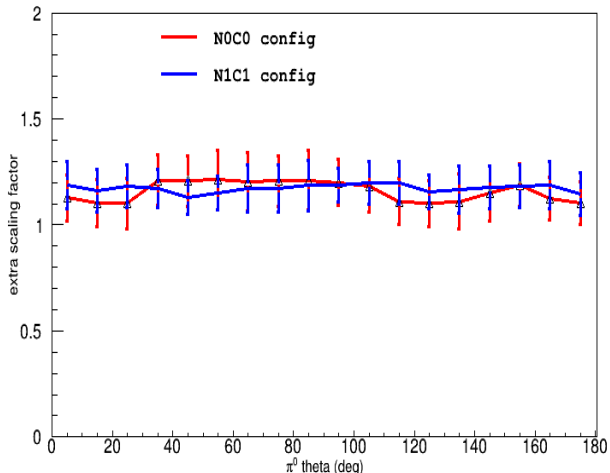
FIG. 7: Example extra carbon scaling factors for negatively polarized target orientation from the 2014 beamtime.

3. Determination of helium scaling factor

To study the coherent background from ^{4}He refrigeration material surrounding the target, the Monte Carlo (MC) simulation on ^{4}He was done using the event generator, EventGen [4]. This was performed for the coherent, ^{4}He(γ, π^0), channel. The output files were passed through the A2 Geant4 simulation and then analyzed with the A2 GoAT physics class [3], followed by the users physics class as the data. In addition, the MC simulation of π^0 photoproduction using a normal proton target was also performed. The missing mass distribution from these two simulations were subtracted to determine the ^{4}He scaling factor. These factors were then applied to π^0 asymmetry studies. Furthermore, the sum of the two MC simulations, coherent background from ^{4}He and background from proton target for π^0 photoproduction process have been added to show an expected distribution as in Fig. 8.

D. Missing mass for π^0 photoproduction events

The following section shows missing mass studies for π^0 photoproduction events from both the 2014 and 2015 beamtimes. The analysis of missing mass is one of the most powerful steps to address background not eliminated by invariant mass analysis (see Sec. III B). The data analysis was carried out separately for four beam-target configurations, and each of the configurations was divided in to eighteen angular bins: $\theta_{\pi^0} = 0 - 10°$, $10 - 20°$, ..., $170 - 180°$. See [2] for complete details on further data selection criteria and various kinematic cuts on the $\gamma p \to p\pi^0$ reaction channel.

The frozen spin target contains carbon and oxygen in the butanol plus the liquid helium as a cryogen, and they contribute a major source of background in the experiment. In addition to the competing background from pion photoproduction off the proton, this target allows for both coherent Compton scattering and pion photoproduction off of these additional nuclei. Therefore, a separate data run was taken with a carbon target by inserting it into the same cryostat to account for the background from heavy nuclei. It is very important to insert the carbon target into the same target cell because the subtraction removes any contribution from the windows, and/or shells of the cryostat material. Although this was done, the carbon subtraction has not worked well in many experiments [4, 5].

Over the past few years, there have been discussions within the collaboration on the requirement of having separate helium target data and including it in the data analysis to address the background from ^{4}He refrigeration material. For this analysis the separate scaling factor is determined from simulation of coherent π^0 pro-

duction on ^{4}He (Sec. III C 3). To do this, MC simulation of events for a normal proton target on π^0 photoproduction process and for a helium target on coherent process were generated as discussed in Sec. III C 3. The sum of the π^0 photoproduction and helium contributions have been used to show expected distributions. Fig. 8 shows an example missing mass spectrum at $\theta_{\pi^0} = 50 - 60°$ for the N1C1 (see Appendix A for nomenclature details) beam-target configuration from the 2015 beamtime. As the agreement between the experimental missing mass and sum of the two simulations, π^0 photoproduction and helium, is rather good, the expected distributions are used for comparison at every angular bin and over all π^0 angles.
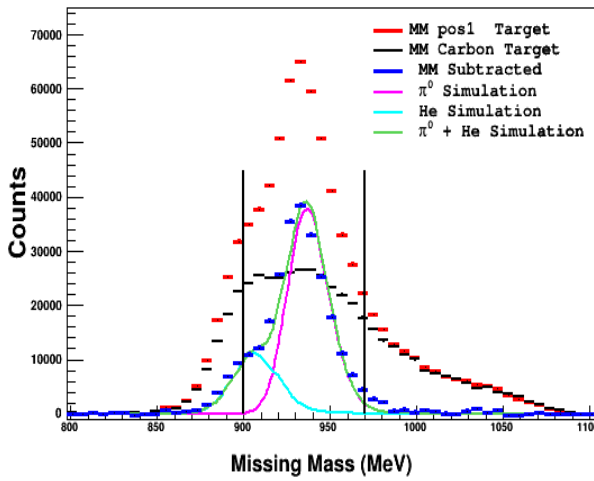
FIG. 8: Missing mass spectra at $\theta_{\pi^0} = 50 - 60°$ and $E_\gamma = 310 - 330$ MeV for the π^0 photoproduction channel from the 2015 beamtime. The two vertical lines represent the missing mass integration limit.

Furthermore, the missing mass spectra were studied over all θ_{π^0} angles and all four beam-target orientations for both the 2014 and 2015 beamtimes and the results are included in Appendix A (Figs. 31– 38).

E. Target Polarization for 2014 Beamtime

The precise knowledge of target polarization is essential for the determination of π^0 and Compton $\sum_{2z}$ asymmetries because these values enter as a normalization factor in the asymmetry formula. Several checks including target polarization studies were carried out after submitting the Compton paper for internal review. Detailed investigation of the target polarization correction was suggested by some of the members of the collaboration because the target polarization values used initially
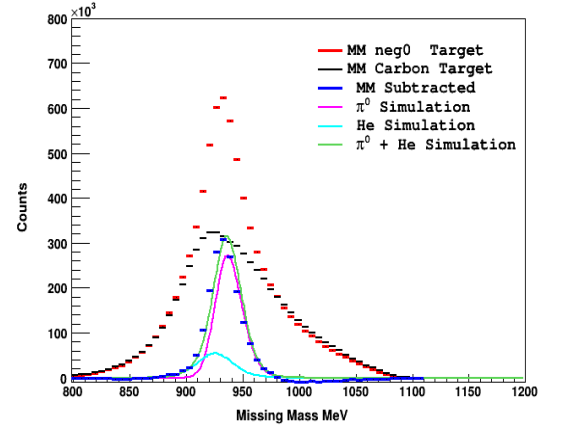

FIG. 9: Missing mass spectra over all θ_{π^0} angles at $E_\gamma = 285 - 305$ MeV for the π^0 photoproduction channel from the 2015 beamtime.

were too small compared to what has been measured in the past. In addition, other groups including the target group and the Bonn group independently carried out studies to address polarization issues for all of the data taken from May 2013 to September 2015.

As part of the investigation from our Compton group, the target polarization values were cross checked with material in Ref.[2]. Table I shows the target polarization measurements for the 2014 beamtime [5]. To further investigate the target polarization corrections, the target group coordinator was requested to reproduce the polarization measurements for the 2014 beamtime. Table II shows the reproduced polarization values [7, 8]. These target polarization measurements reproduced in March 15, 2018, for the 2014 beamtime were slightly different compared to those included previously in [2]. However, the difference is rather small and is within the limits of the systematics: on the order of 1.5%. Therefore the polarization values included in Ref.[2] were applied in this target polarization correction study.

Start date	End date	$P_i^T (\%)$	$P_f^T (\%)$	$1.4P_i^T (\%)$	$1.4P_f^T (\%)$
02.05.2014	12.05.2014	64.31	59.80	90.03	83.72
13.05.2014	19.05.2014	-63.45	-55.04	-88.83	-77.01

TABLE I: Summary of target polarization at the start and end of the data taking periods [5] with extra corrections [9] for the 2014 beamtime.

The target group reported the polarization issues at the 2016 March Collaboration meeting [1], and their study found that the polarization correction factors are needed because there was an extra layer of ice (Fig. 10) for the data taken from May 2013 to September 2015.

Start date	End date	$P_i^T(\%)$	$P_f^T(\%)$	$1.4P_i^T(\%)$	$1.4P_f^T(\%)$
02.05.2014	12.05.2014	63.6	58.7	89.04	82.18
13.05.2014	19.05.2014	-61.6	-53.7	-84.84	-75.18

TABLE II: Summary of target polarization at the start and end of the data taking periods [7, 8] and suggested corrections [9] for the 2014 beamtime.

The target polarization correction factors are: 1.4 for the 2014 and 1.15 (GE experiment) for 2015 beamtimes respectively. These values were also independently reproduced by the Bonn group [9]. Table II shows the actual target polarization, and polarization values after applying these corrections. Target polarization measurements are not possible during data taking because the polarizing magnet does not fit in the geometry of the CB detector. Moreover, the magnetic field strength and homogeneity of the holding coil is not sufficient for polarization measurements. Therefo re, the maximum polarization, P_i, at the start of the data taking period and final polarization, P_f, at the end of the data taking period, for separate target polarization orientations are included. It should be pointed out that the polarization did not drop below 50% over the data taking period for either orientation, and thus repolarization of the target was not required.
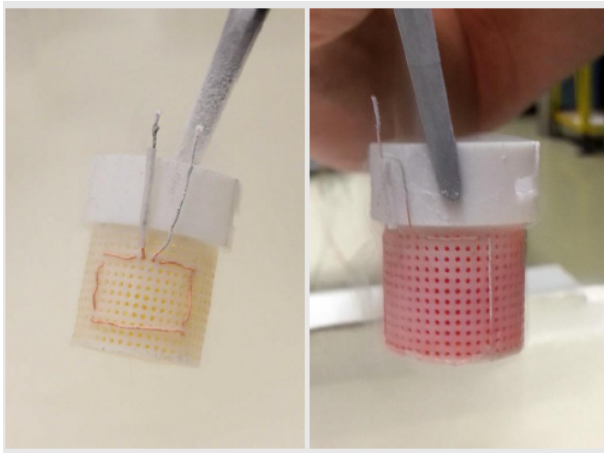

FIG. 10: Proton NMR coils for May 2014 (left) and for May 2015 (right) beamtime [1, 7]

.

F. Target Polarization for 2015 Beamtime

The target polarization measurements for the 2015 beamtime are shown in Table III [7]. The corrected target polarization values after applying corrections discussed in Sec. III E are as shown in the fifth and sixth columns of Table III.

Start date	End date	$P_i^T(\%)$	$P_f^T(\%)$	$1.15P_i^T(\%)$	$1.15P_f^T(\%)$
23.06.2015	02.07.2015	74.23	62.72	85.36	72.13
02.07.2015	11.07.2015	-65.16	-49.04	-74.75	-56.40

TABLE III: Summary of target polarization at the start and end of the data taking periods [7] including those corrections discussed in Sec. III E for the 2015 beamtime.

IV. $\pi^0 \sum_{2z}$ ASYMMETRY RESULTS

The π^0 photoproduction reaction, compared to Compton scattering, is a relatively background-free signal due to its large cross section and the CB-TAPS experimental set-up. However, it is important to apply various kinematic cuts and correct scaling factors. The π^0 photoproduction asymmetries as a function of π^0 angle from both the 2014 and 2015 beamtimes are shown in Fig. 11. The helium correction factor determined from the MC simulation (see Sec. V A) was applied and the results were compared with SAID [10] and MAID models [11]. The π^0 asymmetry results indicate that the extra correction factors are needed.
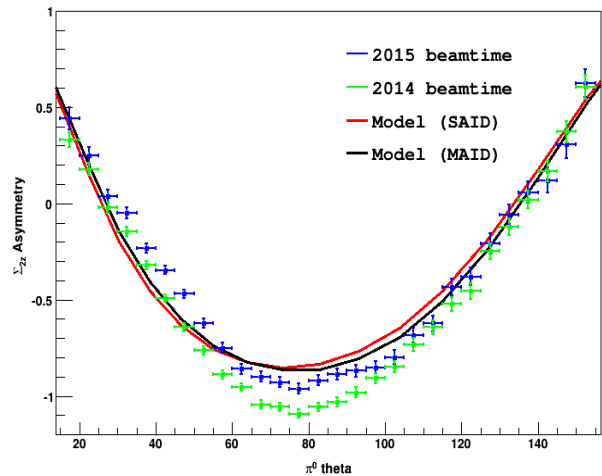

FIG. 11: π^0 asymmetry results without the extra target polarization correction factors at $E_\gamma = 285 - 305$ MeV.

Fig. 12 shows the π^0 asymmetry results including the target polarization correction factors (1.26 ± 0.03 and 1.12 ± 0.02 for the 2014 and 2015 beamtimess respectively). These factors were determined by minimizing
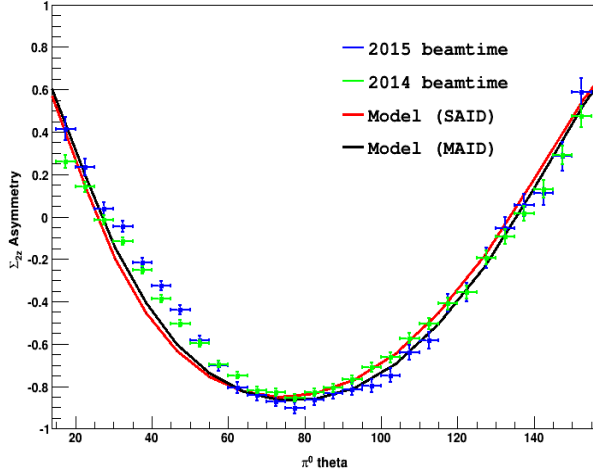
FIG. 12: π^0 asymmetry results with an extra target polarization factor (1.26 and 1.12 from the 2014 and 2015 beamtimes, respectively) applied at $E_\gamma = 285 - 305$ MeV.

the χ^2 per degree of freedom for both the 2014 and 2015 beamtimes. The average of the SAID and MAID models was also determined. It is clearly seen that the $\sum_{2z}$ asymmetry results for the π^0 photoproduction events are in good agreement (within the statistical uncertainties) with both the SAID and MAID models after applying these extra correction factors at the given energy range. This agreement with the SAID and MAID models provides justification for the applied correction factors. This factor is cross checked from polarized and unpolarized cross section studies and is presented in Sec. V.

V. POLARIZED AND UNPOLARIZED CROSS SECTION

The determination of an asymmetry on the longitudinally polarized butanol target, either for the Compton scattering process of interest or for the π^0 photoproduction process used above to extract a polarization correction factor, suffers from one point also addressed above. For the butanol target data, the background contribution from the reactions produced on C, O, and He nuclei could not be fully separated from the polarized H contribution. As these backgrounds from spinless nuclei are not polarization dependent, they cancel when the difference between events in the 3/2 (parallel orientation in Figs. 1a and 1d) and 1/2 (antiparallel orientation in Figs. 1b and 1c) helicity states is taken [13], where 3/2 and 1/2 indicate the relative nucleon-photon spin con-

figuration for parallel and anti-parallel configurations, respectively. The total cross section for parallel ($\sigma^{3/2}$) and anti-parallel ($\sigma^{1/2}$) configurations can be written in terms of unpolarized cross section (σ_0) as,

$$\sigma^{3/2} = \sigma_0 + P_z^t \times P_{circ}^\gamma \times A, \qquad (4)$$

$$\sigma^{1/2} = \sigma_0 - P_z^t \times P_{circ}^\gamma \times A. \qquad (5)$$

The cross section difference ($\Delta\sigma$) between these two helicity states can be written as

$$\Delta\sigma = \sigma^{3/2} - \sigma^{1/2} = 2 \times P_z^t \times P_{circ}^\gamma \times A. \qquad (6)$$

On the other hand, the cross section sum ($\Sigma\sigma$) of the two helicity states cancels out the polarization dependent term, leaving only the unpolarized cross section.

$$\Sigma\sigma = \sigma^{3/2} + \sigma^{1/2} = 2 \times \sigma_0 \qquad (7)$$

For this reason, in the following text the sum of the cross sections will be called the "unpolarized" cross section, and the difference will be called the "polarized" cross section (despite this not being entirely accurate).

Using these two calculations, a cross check of the polarization correction determined above can be provided. Two reactions were studied, the single π^0 photoproduction and the total inclusive cross section, accounting for any and all photoreactions on the target. The analysis method for selecting single π^0 photoproduction is the same as used in the asymmetry analysis outlined previously. The analysis method for a total inclusive analysis entails simply counting hits in the tagger, after accounting for accidentals with the typical sideband subtraction.

Figs. 13 and 14 show the total inclusive unpolarized and polarized cross section results respectively from the 2014 and 2015 beamtimes. The polarized cross section results are also compared with previous data taken to extract the Gerasimov-Drell-Hearn (GDH) sum rule [14].

Similarly, the unpolarized and polarized π^0 cross section results from the 2014 and 2015 beamtimes are shown in Figs. 15 and 16, respectively. The polarized π^0 cross section results are compared with similar GDH data, as well as with the SAID CM12 solution [10].

It is notable that both the total inclusive and π^0 polarized cross sections for the 2014 beamtime appear high compared to the GDH data. This would seem to verify that the polarization values used are incorrect. However, the 2015 cross sections appear low compared to the GDH data. While a lower than actual polarization measurement is realistic, a higher than actual measurement is unexplainable. However, the unpolarized cross
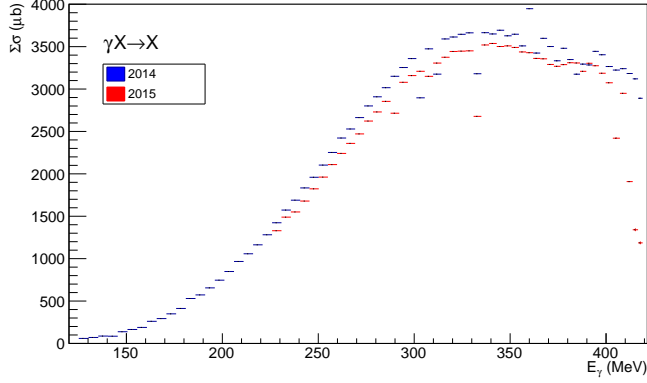
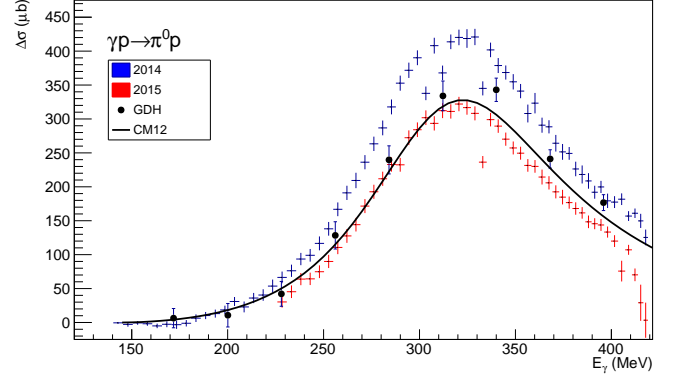FIG. 13: Unpolarized total inclusive cross section results for 2014 (blue) and 2015 (red) beamtimes.
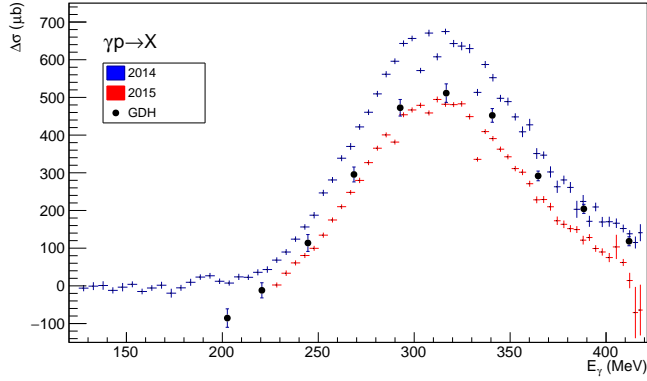

FIG. 14: Polarized total inclusive cross section results for 2014 (blue) and 2015 (red) beamtimes, along with previous GDH data (black circles).
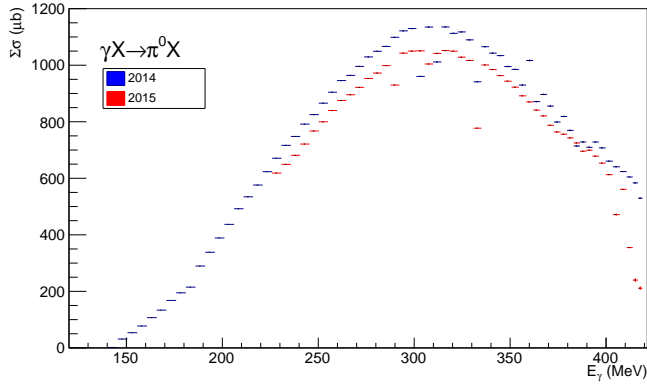

FIG. 15: Unpolarized π^0 cross section results for 2014 (blue) and 2015 (red) beamtimes.

FIG. 16: Polarized π^0 cross section results for 2014 (blue) and 2015 (red) beamtimes, along with previous GDH data (black circles), and the SAID CM12 solution (black line).

sections for 2015 also appear low with respect to their 2014 counterparts. Since these by definition are not influenced by the target polarization, another effect must be the cause. The difficulty with a cross section calculation, as opposed to an asymmetry, is the need to account for the photon flux, target density, target length, and detection efficiencies. While the photon flux is determined for each beamtime separately, the other three: target density, target length, and detection efficiencies are determined only once for all the beamtimes. Therefore, if one of those values changed for 2015 as compared to the 2014, this would result in a decrease in both the unpolarized and polarized cross sections for 2015. While there is no comparison with previous data or theory for the unpolarized cross sections, as they are determined for the total helium immersed butanol target, the unpolarized 2015 cross sections can at least be scaled up to match the 2014 results. This scale factor can be determined by simply taking the ratio of the 2014 to 2015 data, as shown in Fig. 17.

Assuming the need for a scale factor arises from a change in the tagging efficiency, target density, or other quantity that is independent of the incoming photon energy, E_γ, it's reasonable to simply fit these ratios with a flat line. To improve this fit, several channels were manually removed where that channel was significantly discrepant from its neighbors in either 2014 or 2015, as this then led to an unreasonable scale factor for that channel. This fitting then gives scale factors of 1.058 and 1.074 for the total inclusive and π^0 reactions, respectively. Figs. 18 and 19 show the total inclusive and π^0 unpolarized cross section results from the 2014 and 2015 beamtimes, respectively, where these scaling factors have been applied to the 2015 data.

To determine the polarization related scaling factor, the ratio of the 2014 to 2015 polarized cross sections can
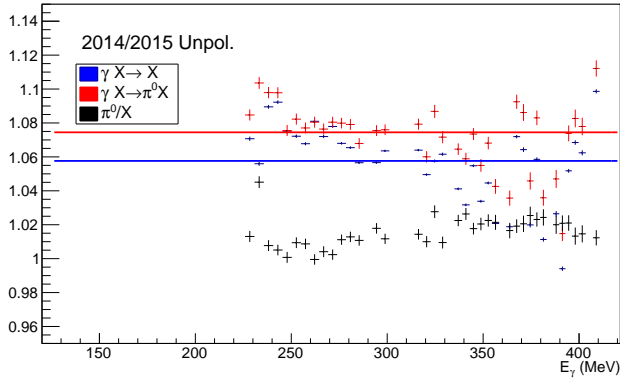
FIG. 17: Ratio of 2014/2015 unpolarized cross section results for total inclusive (blue) and π^0 production (red), as well as the ratio of these two ratios (black).
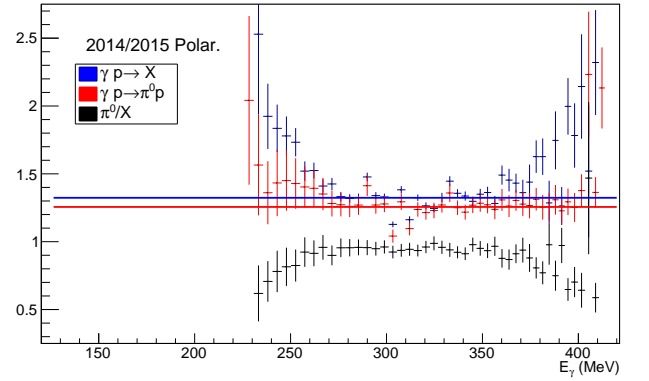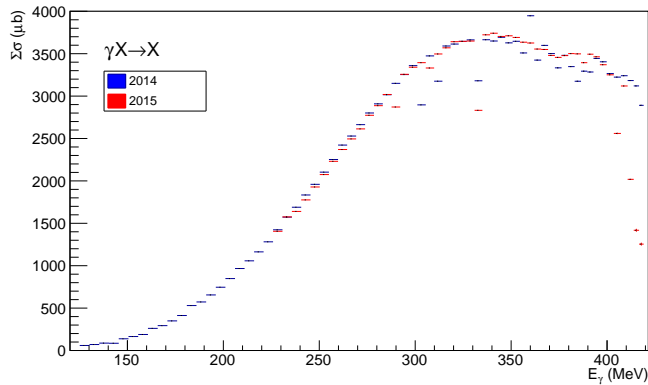

FIG. 18: Unpolarized total inclusive cross section results for 2014 (blue) and 2015 (red) beamtimes, where the latter is scaled by 1.058.
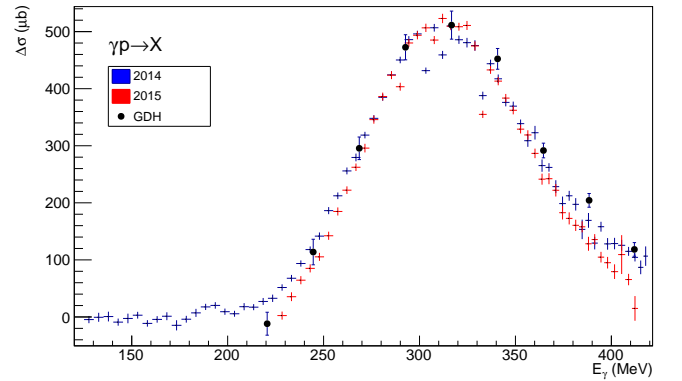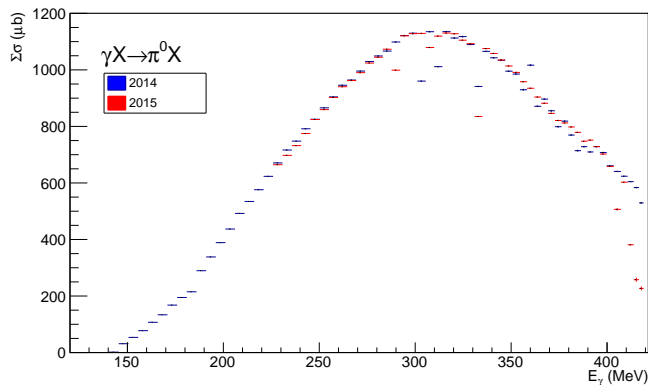

FIG. 19: Unpolarized π^0 cross section results for 2014 (blue) and 2015 (red) beamtimes, where the latter is scaled by 1.074.

FIG. 20: Ratio of 2014/2015 polarized cross section results for total inclusive (blue) and π^0 production (red), as well as the ratio of these two ratios (black).

FIG. 21: Polarized total inclusive cross section results for 2014 (blue) and 2015 (red) beamtimes, where the former is scaled by 1.323 and the latter by 1.058, along with previous GDH data (black circles).

also be constructed, after first applying the previous scale factor to the 2015 data. This ratio is shown in Fig. 20, and again fit with a simple straight line as a polarization scale factor should be energy independent.

The extracted factors were then used to scale just the polarized cross sections for the 2014 beamtime. The polarization scale factors for the 2014 beamtime were determined to be 1.323 for the total inclusive case, and 1.256 for the π^0 production case, the latter in clear agreement with the π^0 asymmetry analysis performed above. With both of the 2014 and 2015 scaling factors applied, the polarized data is now in good agreement with the GDH data, as well as with SAID in the case of π^0 photoproduction, as shown in Figs. 21 and 22, for the total inclusive and π^0 production cases respectively.

One concern with this method is that the extracted polarization scale factors are different between the total inclusive and π^0 production cases, which obviously
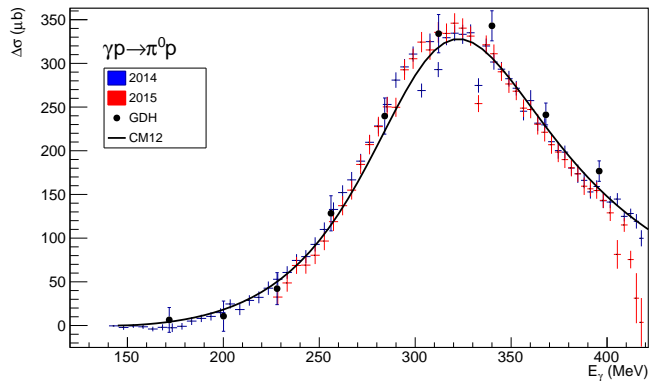
FIG. 22: Polarized π^0 cross section results for 2014 (blue) and 2015 (red) beamtimes, where the former is scaled by 1.256 and the latter by 1.074, along with previous GDH data (black circles), and the SAID CM12 solution (black line).
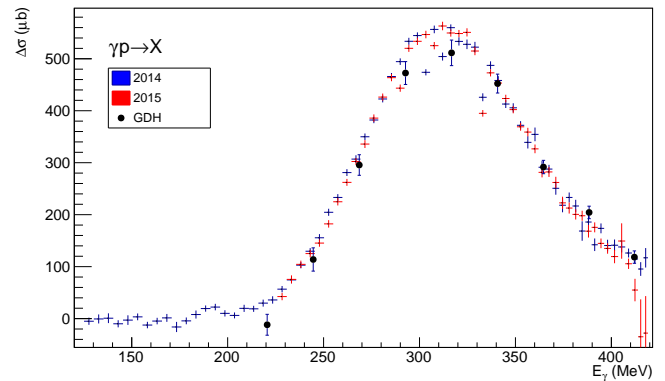

FIG. 24: Polarized total inclusive cross section results for 2014 (blue) and 2015 (red) beamtimes, where the former is scaled by 1.205 and the latter by 1.058 plus a shift of $40\,\mu$b, along with previous GDH data (black circles).
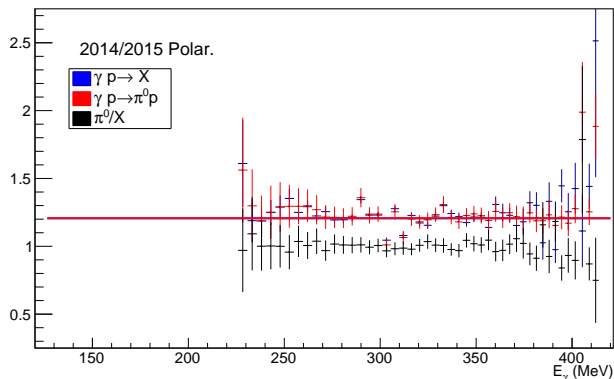

FIG. 23: Ratio of 2014/2015 polarized cross section results for total inclusive (blue) and π^0 production (red), after applying $40\,\mu b$ and $10\,\mu b$ shifts, respectively, as well as the ratio of these two ratios (black).
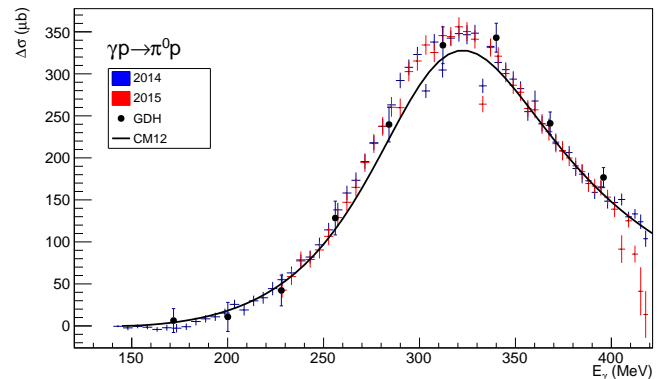

FIG. 25: Polarized π^0 cross section results for 2014 (blue) and 2015 (red) beamtimes, where the former is scaled by 1.208 and the latter by 1.074 plus a shift of $10\,\mu$b, along with previous GDH data (black circles), and the SAID CM12 solution (black line).

shouldn't be the case. Looking into where this discrepancy might arise, the non-linearity of the distributions in Fig. 20 is worrisome. The shapes of the distributions seem to suggest that applying an offset to either the 2014 or 2015 data before taking the ratio might flatten them. This was confirmed by adding $40\,\mu$b and $10\,\mu$b to the 2015 polarized total inclusive and π^0 production cross sections, respectively. Taking the ratios with these data results in flatter distributions, as shown in Fig. 23.

In addition to the flatter distributions, the extracted polarization scale factors of 1.205 and 1.208 for the total inclusive and π^0 production cases, respectively, are in excellent agreement. Applying these shifts and scales to the data results in Figs. 24 and 25.

While the π^0 production results in Fig. 25 still agree

well with both the GDH data and the SAID CM12 solution, the total inclusive results in Fig. 24 are now high with respect to the GDH data in the region around the peak. Regardless, simply shifting the cross sections by these amounts is not justifiable from the analysis standpoint. Initially done as a curiosity, it does however give some indication of the size of the systematic error that should be included with any polarization scale factor derived in this way.

The statistical fitting error is 0.45% and 0.90% for the total inclusive and π^0 production cases, respectively. Although the factor is derived from ratios of cross sections, in which various factors drop out, these factors can be different for each beamtime, so their systematic errors must be accounted for. Combining the relative

systematic errors for beam polarization (2.7%), tagging efficiency (3.2%), target areal density (3.3%), and detection efficiency (taken as 2%), this results in an 8.1% relative error ($5.7\% \times \sqrt{2}$, as the four multiplicative factors are in the numerator and in the denominator). Taking the polarization scale factor derived from the ratio of π^0 production data (without the $10\,\mu$b shift), this gives a factor of $1.256 \pm 0.011\,(\mathrm{stat}) \pm 0.101\,(\mathrm{syst})$, which is well consistent with the other extractions within errors.

A. Comparison of polarization correction factors

The π^0 photoproduction asymmetry $\sum_{2z}$ results discussed in Sec. IV suggest that the target polarization corrections are needed. Tables IV and V show the actual and corrected target polarizations values for the 2014 and 2015 beamtimes determined from MC simulation of coherent π^0 production on ^{4}He. These corrections are similar (within the range of uncertainties) to the factors determined from polarized and unpolarized cross section studies discussed in Sec. V.

Start date	End date	$P_i^T\,(\%)$	$P_f^T\,(\%)$	$1.26P_i^T\,(\%)$	$1.26P_f^T\,(\%)$
02.05.2014	12.05.2014	63.6	58.7	80.13	73.96
13.05.2014	19.05.2014	-61.6	-53.7	-77.61	-67.66

TABLE IV: Summary of target polarization at the start and end of the data taking periods [8] and corrections determined in Sec. IV for the 2014 beamtime.

Start date	End date	$P_i^T\,(\%)$	$P_f^T\,(\%)$	$1.12P_i^T\,(\%)$	$1.12P_f^T\,(\%)$
23.06.2015	02.07.2015	74.23	62.72	83.13	70.24
02.07.2015	11.07.2015	-65.16	-49.04	-72.97	-54.92

TABLE V: Summary of target polarization at the start and end of the data taking periods [7] and corrections determined in Sec. IV for the 2015 beamtime.

VI.   COMPTON $\sum_{2z}$ ASYMMETRY

The $\sum_{2z}$ Compton asymmetry was evaluated by applying various kinematic cuts, including the cuts on missing mass distribution as discussed in [2]. Fig. 44 shows $\sum_{2z}$ Compton asymmetry results from the 2014 and 2015 beamtimes, respectively, at $E_\gamma = 285 - 305$ MeV. The curves are from the fixed-t HDPV dispersion theory calculation of Pasquini, *et al.* [20, 21]. See [2] for details. The polarization correction factors
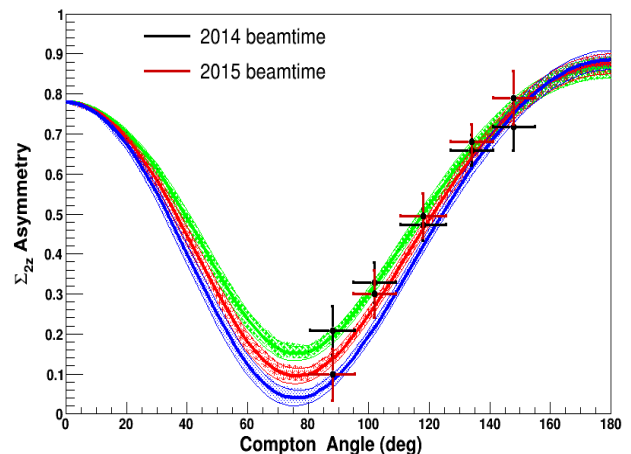

FIG. 26: Compton $\sum_{2z}$ asymmetry (no target polarization correction factor applied) from the 2014 and 2015 beamtime at $E_\gamma = 285 - 305$ MeV.
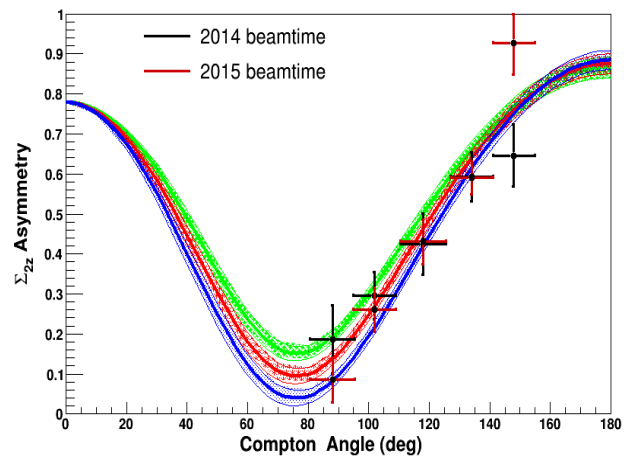

FIG. 27: Compton $\sum_{2z}$ asymmetry with target polarization correction factor applied from the 2014 and 2015 beamtime at $E_\gamma = 285 - 305$ MeV.

from simulation studies discussed in Sec. III C 3 have been applied.

The choice of cut on the upper missing mass limit caused a change in the Compton yield, with a narrow cut eliminating more background but also resulting in a loss of some useful events. A wider cut retains more events, but has a higher possibility of including background. The lower limit in the missing mass cut is 900 MeV/c^2 in each bin. As the target polarization correction factors determined from the π^0 photoproduction process has been applied for Compton scattering, the ratio of the π^0 to Compton in each bin from sim-

Compton Angle	$\Sigma_{2z} \pm \delta\Sigma_{2z}(pt-to-pt)$
88°	0.117 ± 0.046
102°	0.277 ± 0.035
118°	0.428 ± 0.036
134°	0.592 ± 0.026
148°	0.775 ± 0.050

TABLE VI: Compton $\sum_{2z}$ asymmetry results at five Compton angular bins for $E_\gamma = 285 - 305$ MeV. The uncertainties represent the pt-to-pt uncertainty averaged between the 2014 and 2015 beamtimes for each tagged photon energy and angle.

FIG. 28: Weighted average of $\sum_{2z}$ Compton asymmetry final results from the 2014 and 2015 beamtimes at $E_\gamma = 285 - 305$ MeV.

ulation has been used to determine the upper cuts in the missing mass. This resulted tighter missing mass cut and larger statistical uncertaintities compared to [2]. See Appendix B for details on the updated upper cuts in the missing mass. As such, the cuts on the reconstructed proton missing mass were used to extract the $\sum_{2z}$ asymmetry. To extract the systematic uncertainty, the standard cut positions discussed in Appendix B were changed by ± 5 MeV/c² and the $\sum_{2z}$ asymmetry was calculated to extract the relative difference. The shift on the asymmetries was random, i.e. varied up and down randomly from bin-to-bin. This random shift was evaluated to be $\approx \pm 10\%$.

The Compton $\sum_{2z}$ asymmetry results obtained by combining the results from the two beamtimes via their weighted average, are shown in Fig. 45. The uncertainties were handled by separating them into correlated and point-to-point (pt-to-pt) uncertainties. The uncertainty of the experimental parameters: target polarization (3%), beam polarization (2.7%), helium scaling factor and carbon scaling factor are correlated for the measurement of the $\sum_{2z}$ asymmetry, but this is not so for the uncertainty due to the missing mass integration limit. Thus, the systematic uncertainties from the first four sources were added in quadrature (last column of Table VIII in Appendix) and are then plotted as a separate band, corresponding to every Compton angle as in Fig. 45. The uncertainty from the MC simulations of ⁴He and carbon background was estimated in the range $3 - 5\%$ and $4 - 6\%$, respectively. However, the uncertainty from the cuts on the reconstructed proton missing mass is completely random, hence they are summed in quadrature (Table VI) with the statistical uncertainty. These uncertainties were then averaged between the 2014 and 2015 beamtimes seperately corresponding to each tagged photon energies and angles.
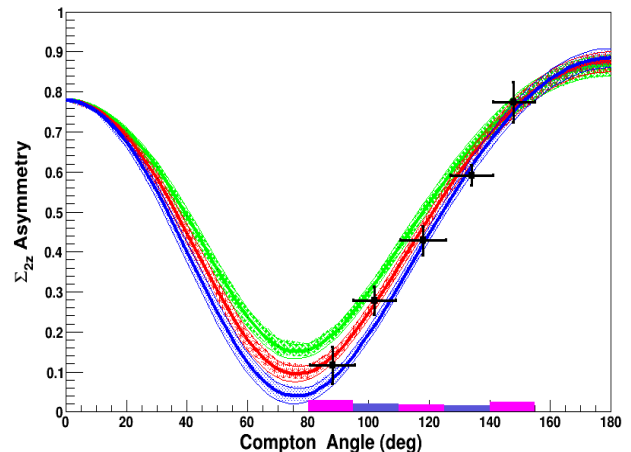
VII.   SUMMARY

In summary, the target correction factors determined, including simulation of coherent π^0 production on ⁴He (Sec. III C 3) and from helicity dependent cross section studies (Sec. V), agree within the statistical uncertainties. This indicates that there are no systematic effects or flaws in the methodology of the data analysis. The agreement suggests that both the simulation of coherent π^0 production on ⁴He and the helicity dependent cross section difference and sum can be used to investigate inconsistencies in target polarization values. The target polarization corrections determined from the ratio of tagger scalers, normalized yield ratio for π^0 chanel and simulation of coherent π^0 production on ⁴He as discussed in Sec. IV were choosen to apply in the analysis of the Compton scattering assymmetries. Although these correction factors have a small impact on the Compton scattering channel, they can not be ignored for the π^0 production channel.

Appendix A   MISSING MASS FOR π^0 PHOTOPRODUCTION EVENTS AT ALL ANGLES

The following naming convention have been used in the following sections.

- P0C0: Positively polarized target (P) with left helicity (0) state of the beam, and carbon target (C) with left helicity (0) state was used in background subtraction.

- P1C1: Positively polarized target (P) with right helicity (1) state of the beam, and carbon target (C) with right helicity (1) state was used in background subtraction.

- N0C0: Negatively polarized target (N) with left helicity (0) state of the beam, and carbon target (C) with left helicity (0) state was used in background subtraction.

- N1C1: Negatively polarized target (N) with right helicity (1) state of the beam, and carbon target (C) with right helicity (1) state was used in background subtraction.

Fig. 31 shows the missing mass spectra for "N0C0" configuration at eighteen angular bins, top left to right: $\theta_{\pi^0} = 0 - 10°$, $10 - 20°, 20 - 30°$ and so on. Similarly, the missing mass spectrum for "N1C1", "P0C0" and "P1C1" configurations are shown in Figs. 32– 38 respectively.

Appendix B   ADDITIONAL PLOTS
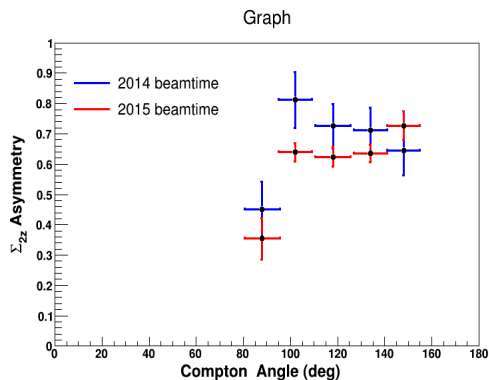
A   Systematic Errors

FIG. 41: Compton $\sum_{2z}$ asymmetry with target polarization correction factor applied from the 2014 and 2015 beamtime at $E_\gamma = 310 - 330$ MeV.
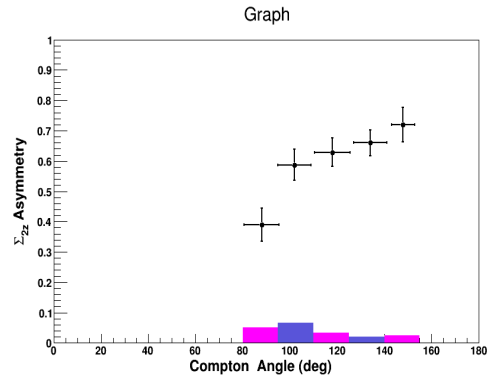

FIG. 42: Weighted average of $\sum_{2z}$ Compton asymmetry results from the 2014 and 2015 beamtimes at $E_\gamma = 310 - 330$ MeV.

Compton Angle	$\Sigma_{2z} \pm \delta\Sigma_{2z}(pt-to-pt)$
88°	0.189 ± 0.066
102°	0.292 ± 0.047
118°	0.402 ± 0.044
134°	0.673 ± 0.042
148°	0.667 ± 0.048

TABLE X: Compton $\sum_{2z}$ asymmetry results at five Compton angular bins for $E_\gamma = 265 - 285$ MeV. The uncertainties represent the pt-to-pt uncertainty averaged between the 2014 and 2015 beamtimes for each tagged photon energy and angle.

Compton Angle	$\Sigma_{2z} \pm \delta\Sigma_{2z}(pt-to-pt)$
88°	0.387 ± 0.046
102°	0.639 ± 0.031
118°	0.624 ± 0.032
134°	0.636 ± 0.028
148°	0.727 ± 0.047

TABLE XI: Compton $\sum_{2z}$ asymmetry results at five Compton angular bins for $E_\gamma = 310 - 330$ MeV. The uncertainties represent the pt-to-pt uncertainty averaged between the 2014 and 2015 beamtimes for each tagged photon energy and angle.

| Beamtime	Compton Angle	Summary of uncertaities ($\pm$)							
		stat	syst-rand (5 − 10%)	pt-to-pt	syst-target (3%)	syst-beam (2.7%)	syst-carbon (4 − 6%)	syst-helium (3 − 5%)	syst-scale
2014	88°	0.091	0.022	0.094	0.007	0.006	0.016	0.011	0.021
	102°	0.070	0.027	0.075	0.008	0.007	0.019	0.013	0.025
	118°	0.048	0.032	0.058	0.012	0.011	0.024	0.020	0.035
	134°	0.033	0.059	0.068	0.020	0.017	0.033	0.026	0.049
	148°	0.083	0.045	0.094	0.022	0.020	0.037	0.030	0.056
2015	88°	0.092	0.016	0.093	0.005	0.004	0.011	0.008	0.015
	102°	0.056	0.025	0.061	0.009	0.008	0.022	0.012	0.028
	118°	0.060	0.032	0.068	0.012	0.011	0.028	0.012	0.035
	134°	0.042	0.034	0.054	0.020	0.018	0.034	0.034	0.055
	148°	0.041	0.038	0.056	0.019	0.017	0.038	0.019	0.049

TABLE VII: Summary of correlated and uncorrelated uncertainty analysis for the Compton $\sum_{2z}$ asymmetry at $E_\gamma = 265 − 285$ MeV.

| Beamtime	Compton Angle	Summary of uncertaities ($\pm$)							
		stat	syst-rand (5 − 10%)	pt-to-pt	syst-target (3%)	syst-beam (2.7%)	syst-carbon (3 − 6%)	syst-helium (3 − 5%)	syst-scale
2014	88°	0.083	0.019	0.085	0.006	0.005	0.011	0.008	0.015
	102°	0.051	0.030	0.059	0.009	0.008	0.015	0.015	0.024
	118°	0.068	0.034	0.076	0.013	0.012	0.017	0.013	0.027
	134°	0.044	0.042	0.060	0.018	0.016	0.024	0.018	0.038
	148°	0.067	0.039	0.077	0.019	0.017	0.019	0.019	0.038
2015	88°	0.056	0.009	0.056	0.003	0.002	0.005	0.004	0.008
	102°	0.049	0.026	0.056	0.008	0.007	0.016	0.013	0.023
	118°	0.044	0.034	0.056	0.013	0.012	0.017	0.013	0.028
	134°	0.033	0.041	0.041	0.018	0.016	0.018	0.018	0.034
	148°	0.062	0.046	0.077	0.028	0.025	0.028	0.028	0.054

TABLE VIII: Summary of correlated and uncorrelated uncertainty analysis for the Compton $\sum_{2z}$ asymmetry at $E_\gamma = 285 − 305$ MeV.

Beamtime	Compton Angle	Summary of uncertaities ($\pm$)							
		stat	syst-rand (6 − 10%)	pt-to-pt	syst-target (3%)	syst-beam (2.7%)	syst-carbon (4 − 6%)	syst-helium (3 − 5%)	syst-scale
2014	88°	0.081	0.045	0.092	0.014	0.012	0.027	0.023	0.040
	102°	0.044	0.081	0.092	0.024	0.021	0.050	0.040	0.071
	118°	0.052	0.051	0.073	0.022	0.019	0.034	0.036	0.059
	134°	0.048	0.057	0.075	0.021	0.019	0.024	0.021	0.051
	148°	0.072	0.039	0.082	0.019	0.017	0.035	0.019	0.041
2015	88°	0.059	0.035	0.069	0.011	0.010	0.026	0.017	0.031
	102°	0.042	0.048	0.063	0.014	0.013	0.021	0.019	0.034
	118°	0.041	0.045	0.061	0.017	0.015	0.028	0.016	0.039
	134°	0.034	0.038	0.051	0.019	0.017	0.025	0.019	0.041
	148°	0.063	0.047	0.079	0.024	0.021	0.031	0.024	0.051

TABLE IX: Summary of correlated and uncorrelated uncertainty analysis for the Compton $\sum_{2z}$ asymmetry at $E_\gamma = 310 − 330$ MeV.
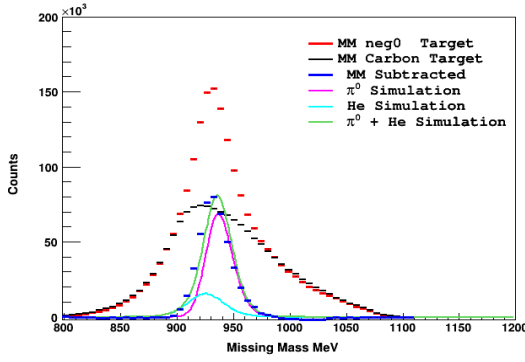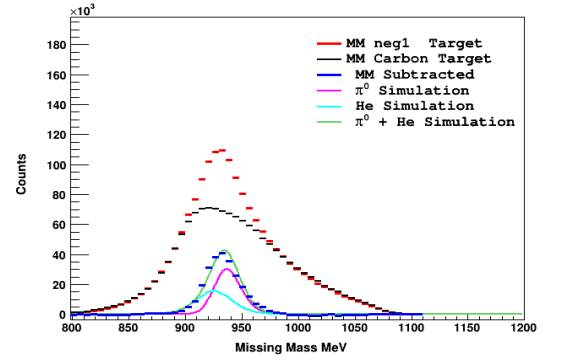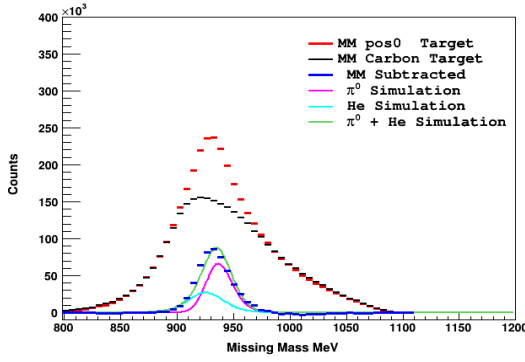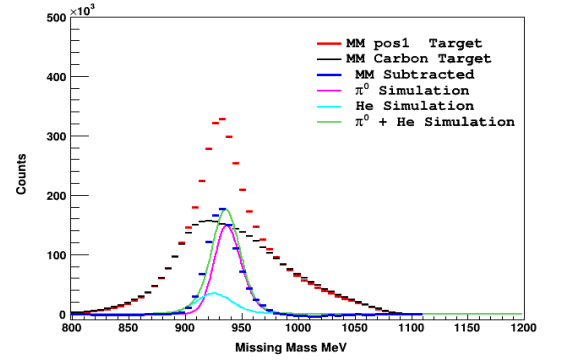
FIG. 29: Missing mass from π^0 photoproduction events over all π^0 angles, and $E_\gamma = 310 - 330$ MeV from the 2014 beamtime. These are the four-fold analysis results on (a) N0CO, (b) N1C1, (c) P0CO and (d) P1C1 parallel and anti-parallel configurations (different target polarization and beam helicity states) as discussed in Sec. III D.
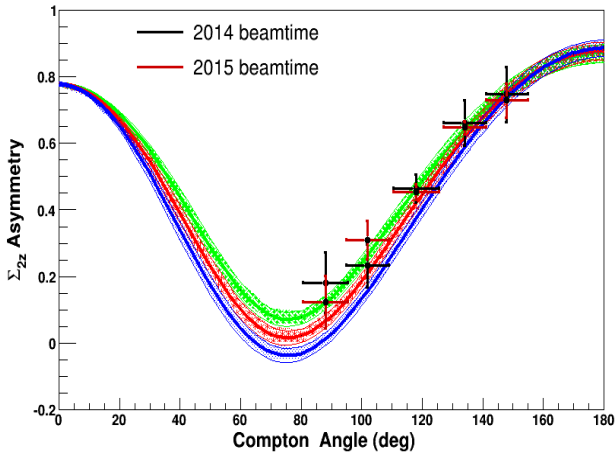
FIG. 43: Compton $\sum_{2z}$ asymmetry (no target polarization correction factor applied) from the 2014 and 2015 beamtime at $E_\gamma = 265 - 285$ MeV.
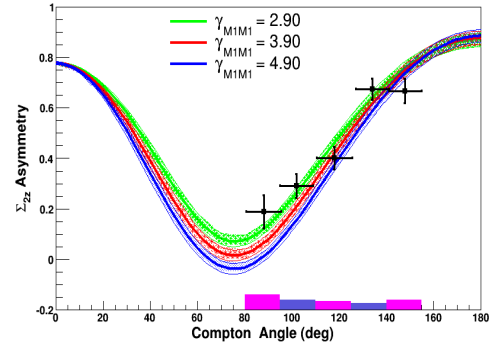
FIG. 45: Weighted average of $\sum_{2z}$ Compton asymmetry results from the 2014 and 2015 beamtimes at $E_\gamma = 265 - 285$ MeV.
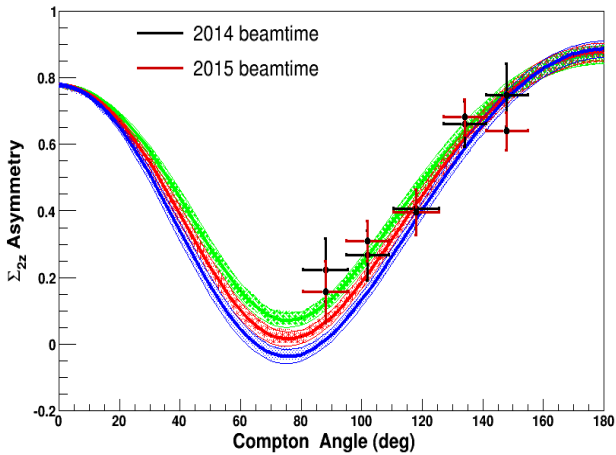
FIG. 44: Compton $\sum_{2z}$ asymmetry with target polarization correction factor applied from the 2014 and 2015 beamtime at $E_\gamma = 265 - 285$ MeV.

[1] G. Reicherz, Collaboration meeting presentation, https://wwwa2.kph.uni-mainz.de/intern/daqwiki/meetings/collaboration_meetings/2016_03/start.
[2] D. Paudyal, Ph.D thesis, University of Regina (2017), http://wwwa2.kph.uni-mainz.de/images/publications/phd/Paudyal-PhD-thesis.pdf.
[3] C. Collicott, *et al.*, in preparation (2018).
[4] P. Martel, *et al.*, Phys. Rev. Lett. **114**, 102501 (2015).
[5] J. Linturi, Internal Report, University of Mainz (2014), https://wwwa2.kph.uni-mainz.de/intern/daqwiki/targetpolarization.pdf.
[6] A. Thomas, Eur. Phys. J. Spec. Top. **198**, 171 (2011).
[7] G. Reicherz, Private Communication.
[8] A. thomas, Private Communication.
[9] F. Afzal, Private Communication.
[10] http://gwdac.phys.gwu.edu/.
[11] https://maid.kph.uni-mainz.de/.

Beamtime	Compton Angular Range	Missing Mass Upper Limit		
		$E_\gamma = 265 - 285$ MeV	$E_\gamma = 285 - 305$ MeV	$E_\gamma = 310 - 330$ MeV
2014	$80 - 95°$	945	948	945
	$95 - 110°$	942	945	945
	$110 - 125°$	943	944	942
	$125 - 140°$	940	942	942
	$140 - 150°$	941	942	945
2015	$80 - 95°$	944	945	945
	$95 - 110°$	941	941	940
	$110 - 125°$	940	942	942
	$125 - 140°$	940	942	940
	$140 - 150°$	940	940	941

TABLE XII: Missing mass cuts determined for three energy and five angular bins of Compton scattering. The upper missing mass limits are based on π^0 photoproduction taken as a reference and detailed Compton $\sum_{2z}$ asymmetry versus upper missing mass limit study.

[12] J. McGeorge, *et al.*, Eur. Phys. J. A **37**, 129 (2008).
[13] J. Ahrens, *et al.*, Phys. Rev. Lett. **84**, 5950 (2000).
[14] J. Ahrens, *et al.*, Phys. Rev. Lett. **87**, 022003 (2001).
[15] A. Thomas, Eur. Phys. J. Spec. Top. **198**, 171 (2011).
[16] V. O. de Leon, *et al.*, Eur. Phys. J. A **10**, 207 (2001).
[17] H. W. Grieβhammer, J. A. McGovern, D. R. Phillips, and G. Feldman, Prog. Part. Nucl. Phys. **67**, 841 (2012).
[18] V. Lensky and V. Pascalutsa, Eur. Phys. J. C **65**, 207 (2010).
[19] S. Kondratyuk, *et al.*, Phys. Rev. C **64**, 024005 (2001).
[20] B. Pasquini, D. Drechsel, and M. Vanderhaeghen, Phys. Rev. C **76**, 015203 (2007).
[21] D. Drechsel, B. Pasquini, and M. Vanderhaeghen, Phys. Rept. C **378**, 99 (2003).
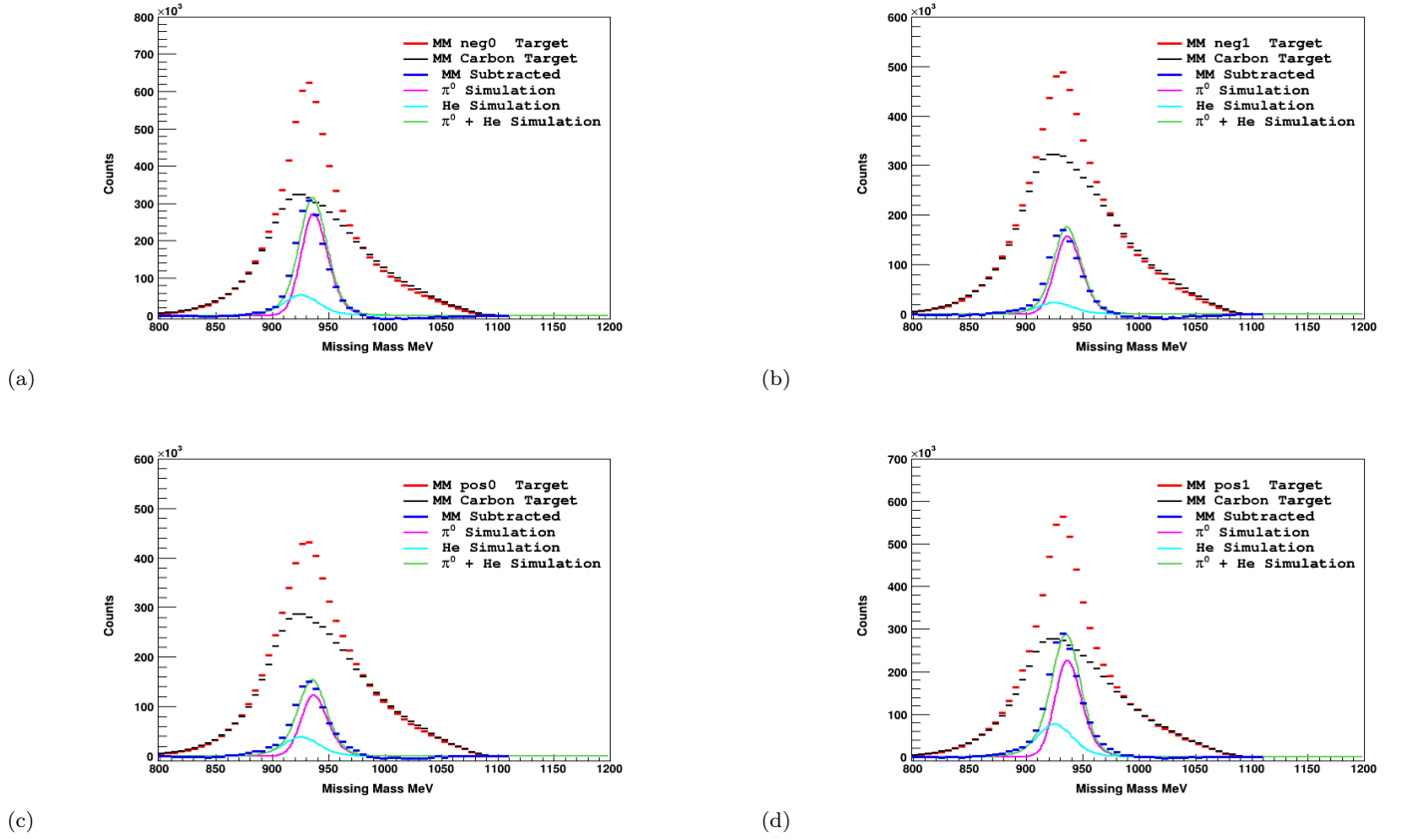
(a)

(b)

(c)

(d)

FIG. 30: Missing mass from π^0 photoproduction events over all π^0 angles, and $E_\gamma = 310 - 330$ MeV from the 2015 beamtime. These are the four-fold analysis results on (a) N0CO, (b) N1C1, (c) P0CO and (d) P1C1 parallel and anti-parallel configurations (different target polarization and beam helicity states) as discussed in Sec. III D.
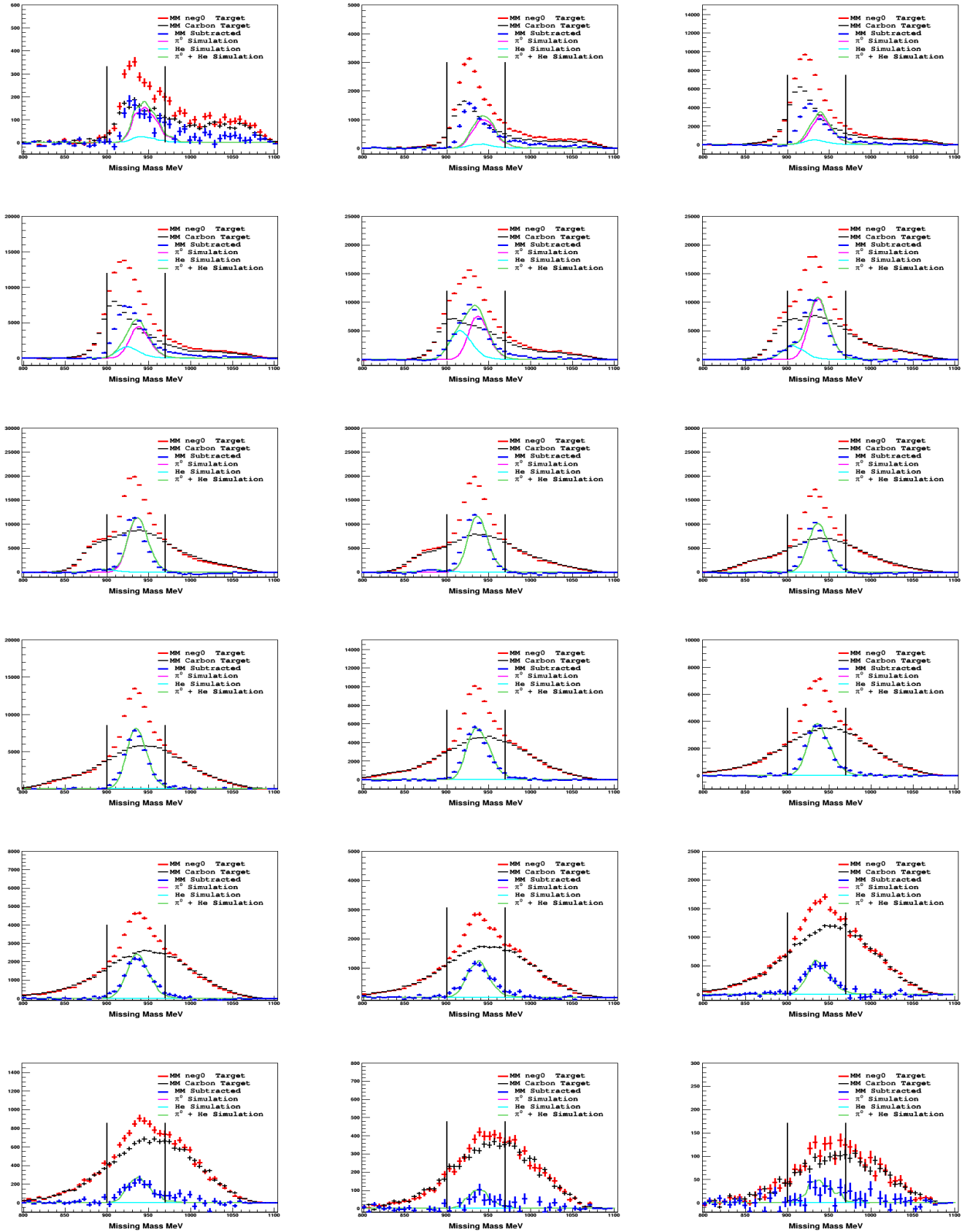
FIG. 31: Missing mass spectrum at $\theta_{\pi^0} = 0 - 10°,\ 10 - 20°, ..., 170 - 180°$ and $E_\gamma = 310 - 330$ MeV on the π^0 photoproduction channel from the 2014 beamtime. The two vertical lines represent the missing mass integration limit (N0C0).
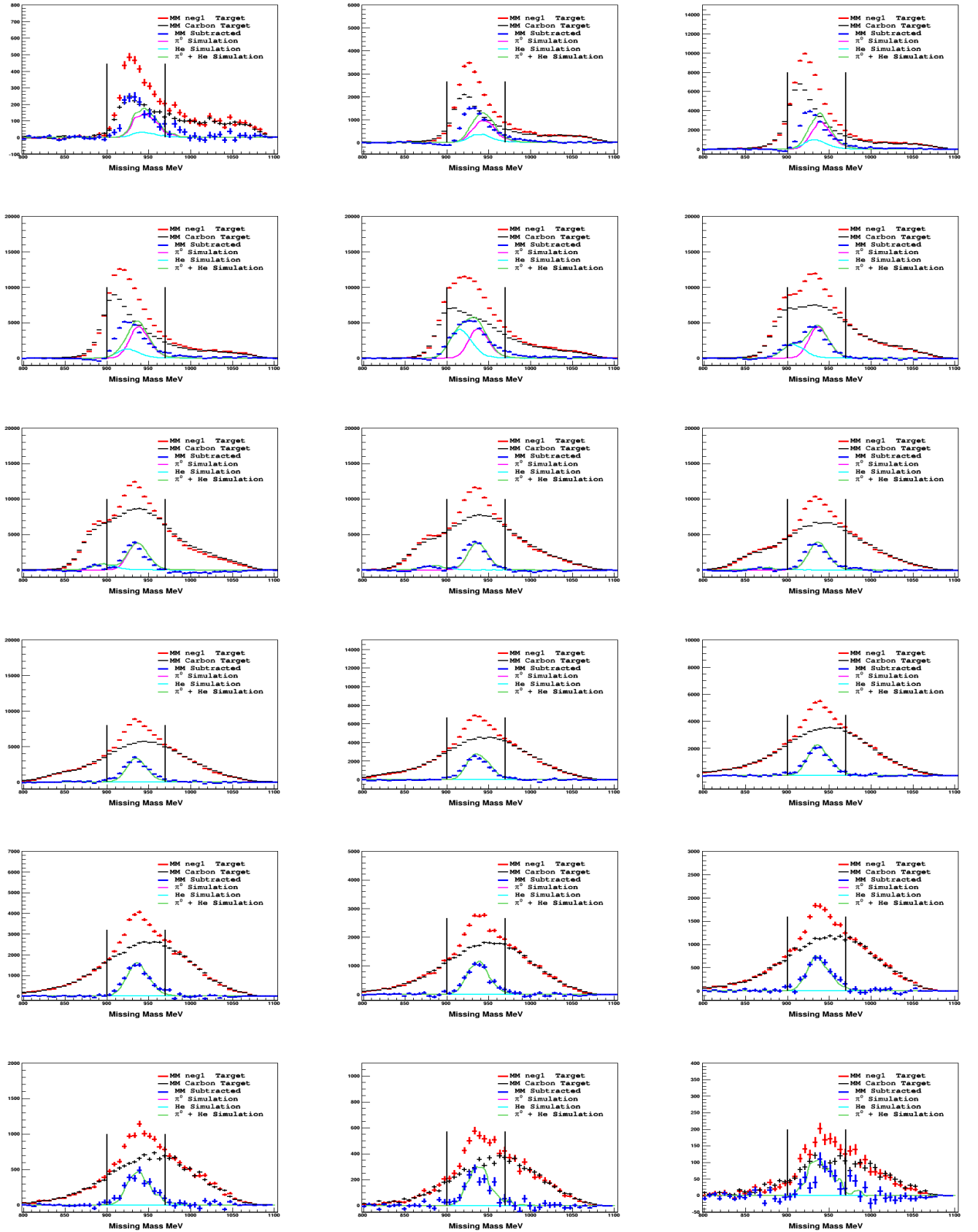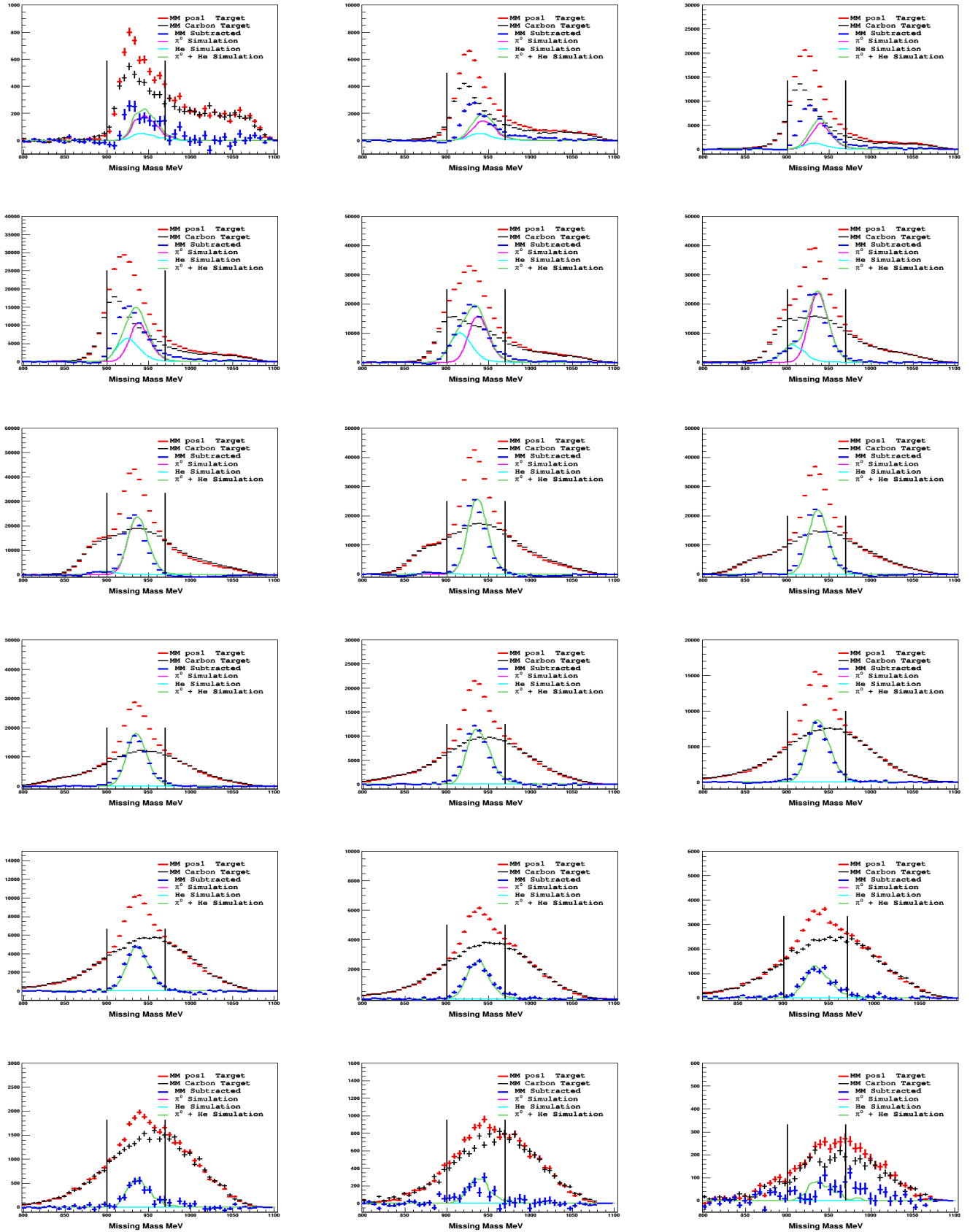
FIG. 32: Missing mass spectrum at $\theta_{\pi^0} = 0 - 10°,\ 10 - 20°, ..., 170 - 180°$ and $E_\gamma = 310 - 330$ MeV on the π^0 photoproduction channel from the 2014 beamtime. The two vertical lines represent the missing mass integration limit (N1C1).
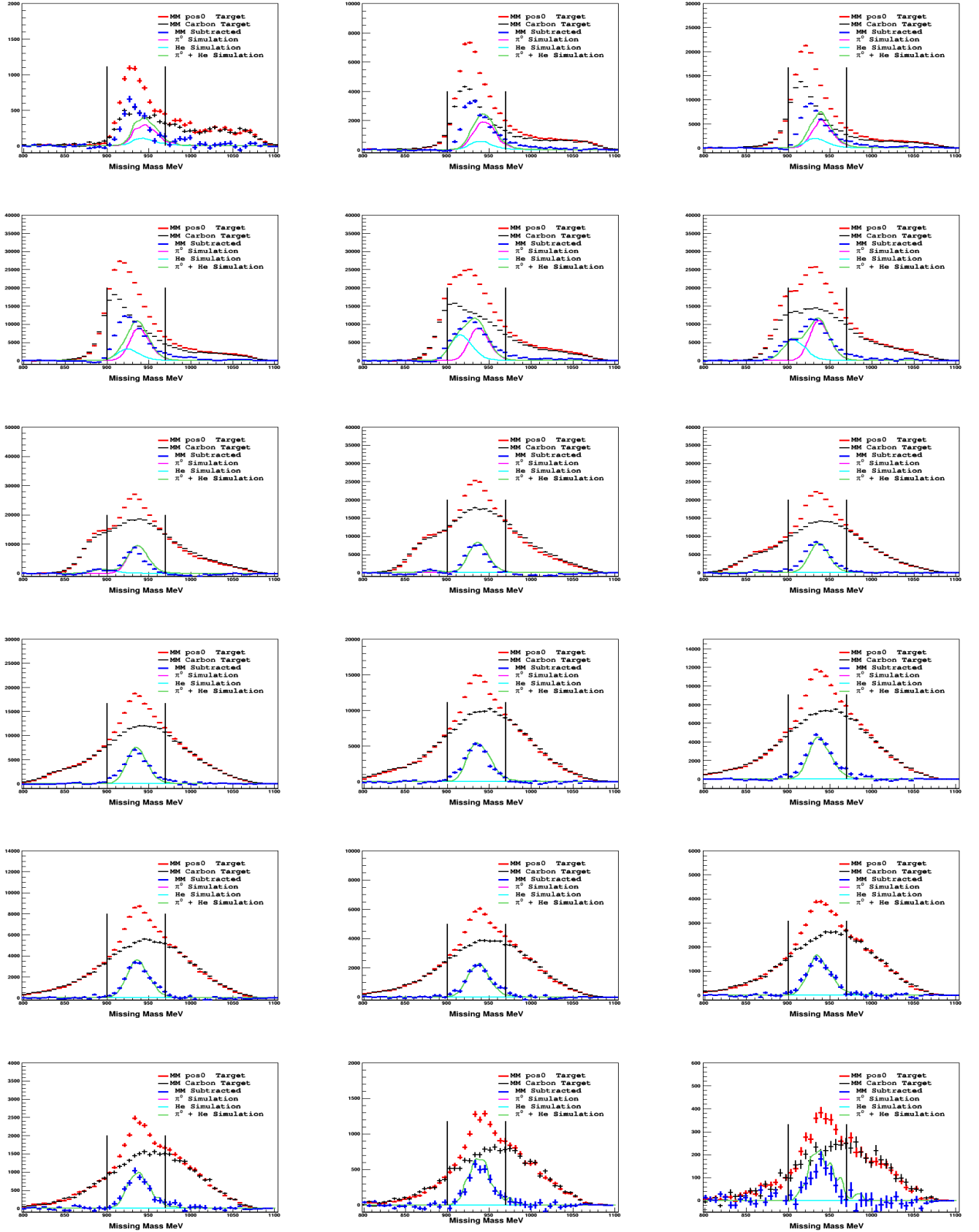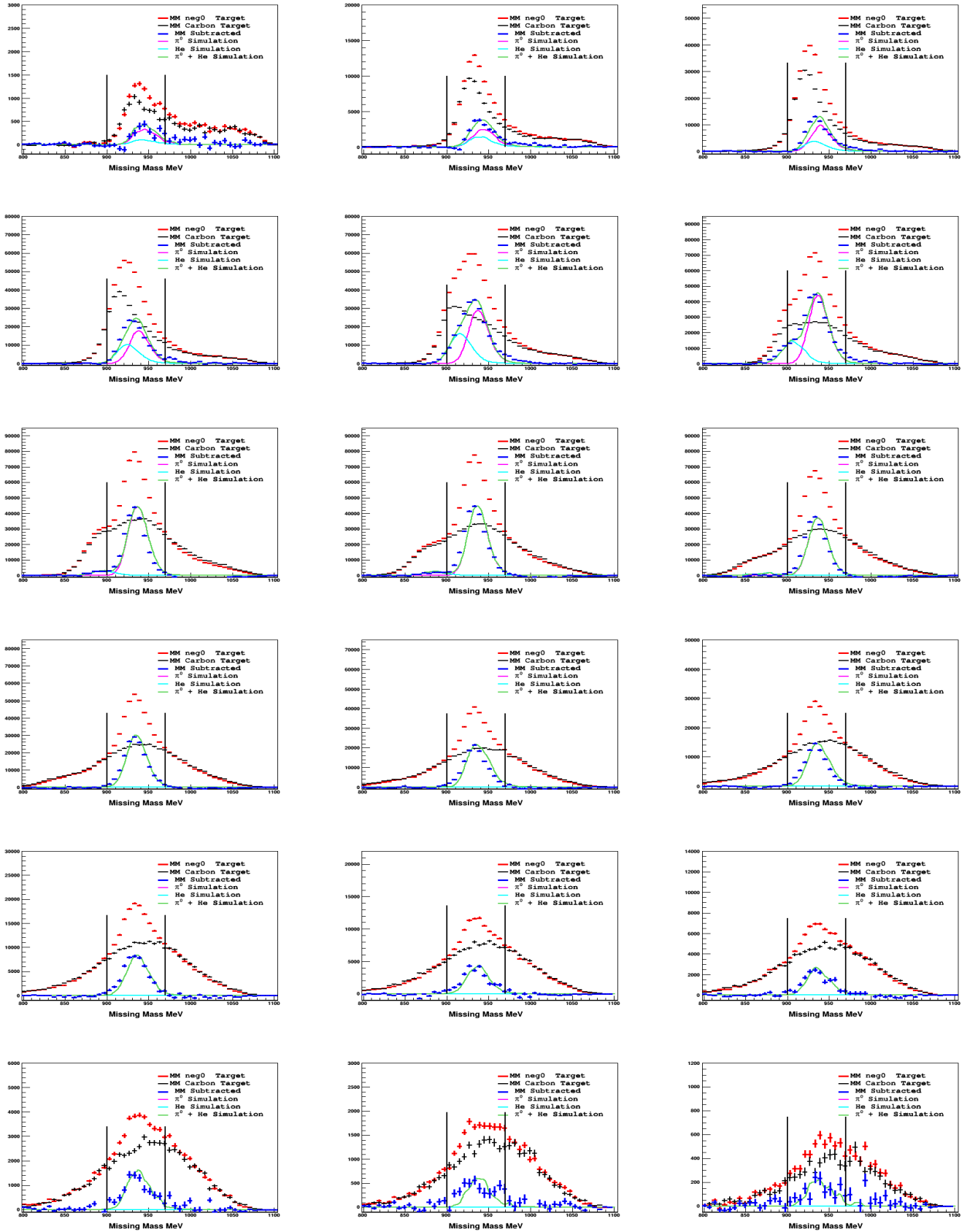
FIG. 33: Missing mass spectrum at $\theta_{\pi^0} = 0 - 10°,\ 10 - 20°, ..., 170 - 180°$ and $E_\gamma = 310 - 330$ MeV on the π^0 photoproduction channel from the 2014 beamtime. The two vertical lines represent the missing mass integration limit (P0C0).
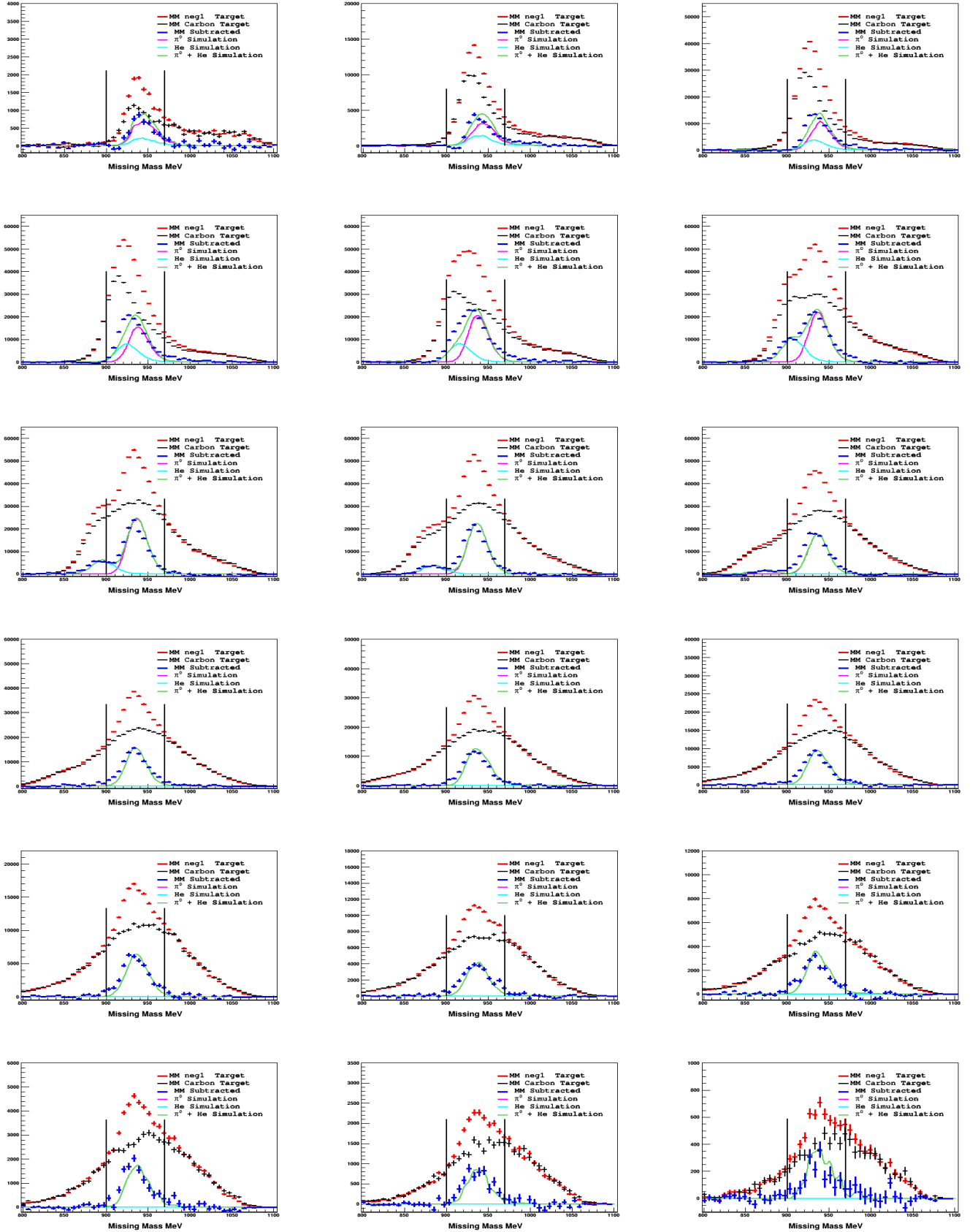
FIG. 34: Missing mass spectrum at $\theta_{\pi^0} = 0 - 10°,\ 10james14 - 20°,....,170 - 180°$ and $E_\gamma = 310 - 330$ MeV on the π^0 photoproduction channel from the 2014 beamtime. The two vertical lines represent the missing mass integration limit (P1C1).

FIG. 35: Missing mass spectrum at $\theta_{\pi^0} = 0 - 10°,\ 10 - 20°, ..., 170 - 180°$ and $E_\gamma = 310 - 330$ MeV on the π^0 photoproduction channel from the 2015 beamtime. The two vertical lines represent the missing mass integration limit (N0C0).
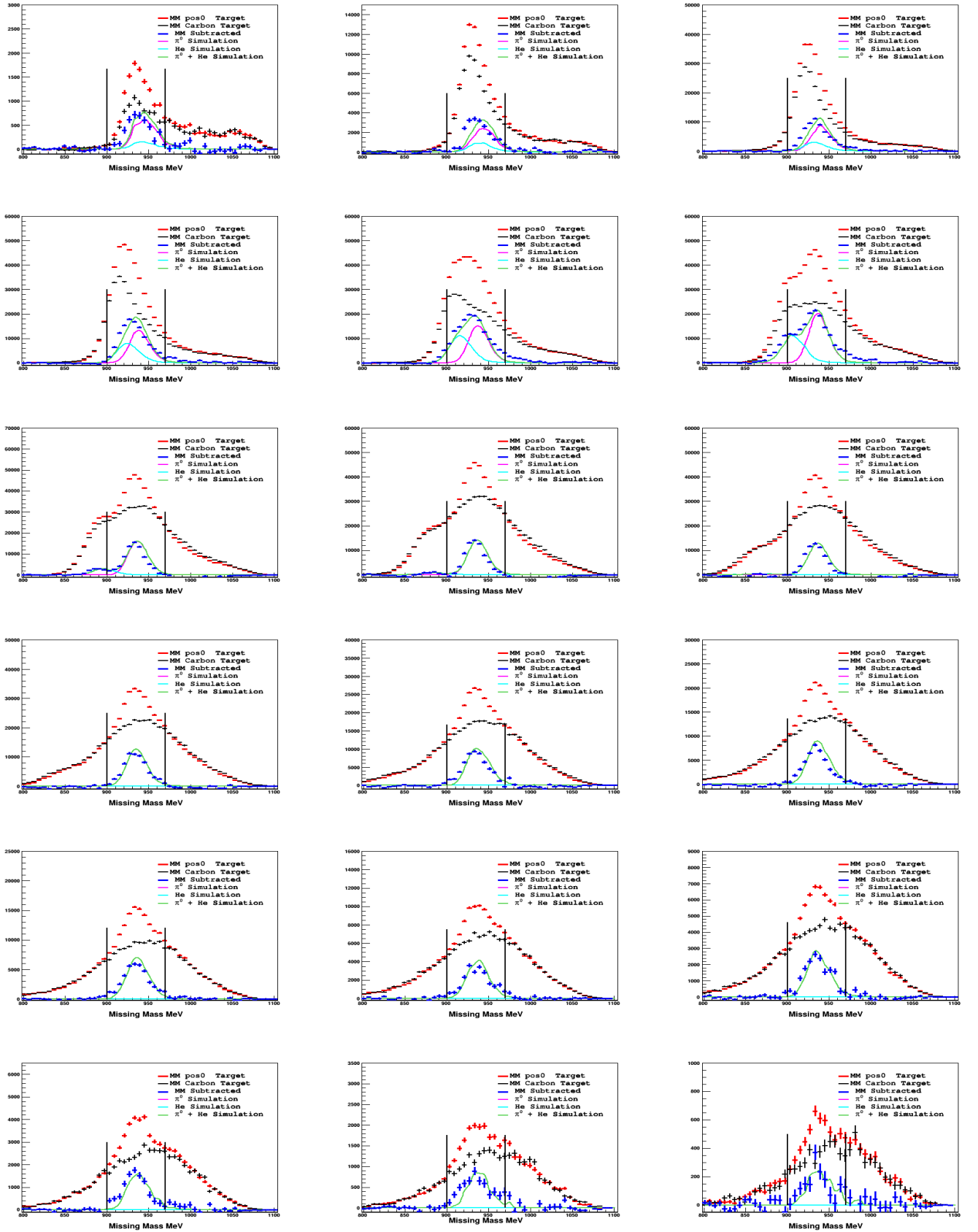
FIG. 36: Missing mass spectrum at $\theta_{\pi^0} = 0 - 10°,\ 10 - 20°, ..., 170 - 180°$ and $E_\gamma = 310 - 330$ MeV on the π^0 photoproduction channel from the 2015 beamtime. The two vertical lines represent the missing mass integration limit (N1C1).
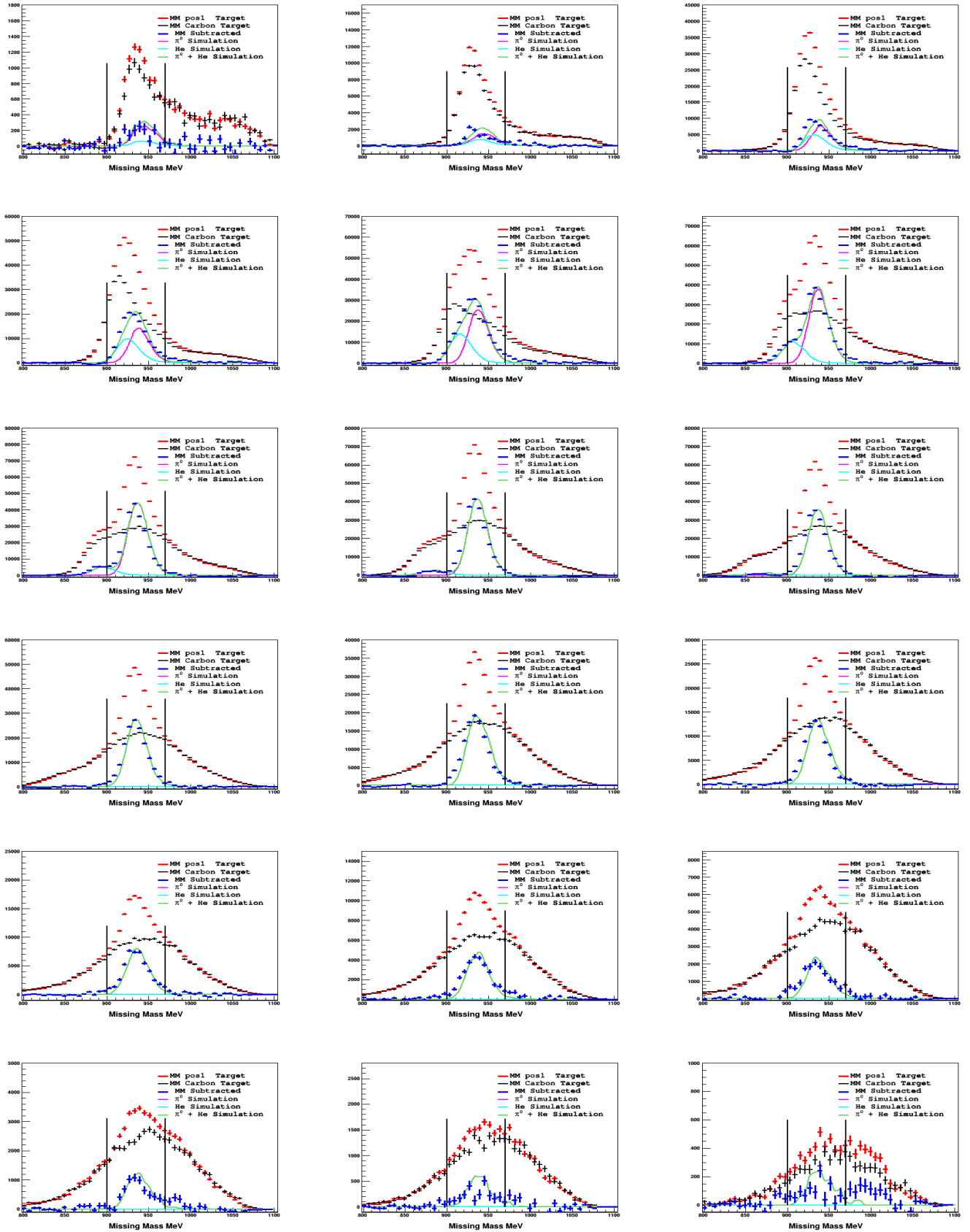
FIG. 37: Missing mass spectrum at $\theta_{\pi^0} = 0 - 10°, \; 10 - 20°, ..., 170 - 180°$ and $E_\gamma = 310 - 330$ MeV on the π^0 photoproduction channel from the 2015 beamtime. The two vertical lines represent the missing mass integration limit (P0C0).

FIG. 38: Missing mass spectrum at $\theta_{\pi^0} = 0 - 10°, \ 10 - 20°, ..., 170 - 180°$ and $E_\gamma = 310 - 330$ MeV on the π^0 photoproduction channel from the 2015 beamtime. The two vertical lines represent the missing mass integration limit (P1C1).
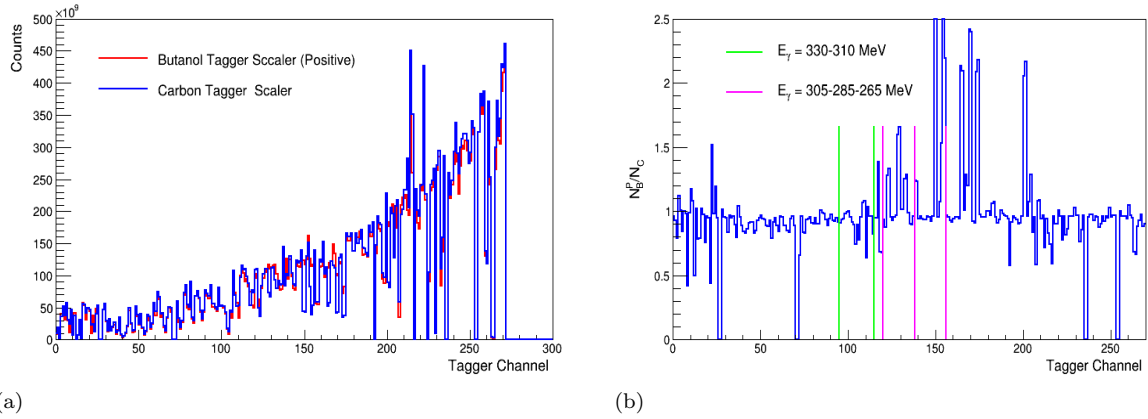
(a)

(b)

FIG. 39: (a)Tagger scaler distribution for positively polarized butanol target and carbon target runs. (b) Ratio of butanol tagger scalers (positively polarized target orientation) to carbon tagger scalers. The vertical lines show the tagged energy range of interest corresponding to tagger channels. The fluctuations represent missing tagger channels and the statistical fluctuations.
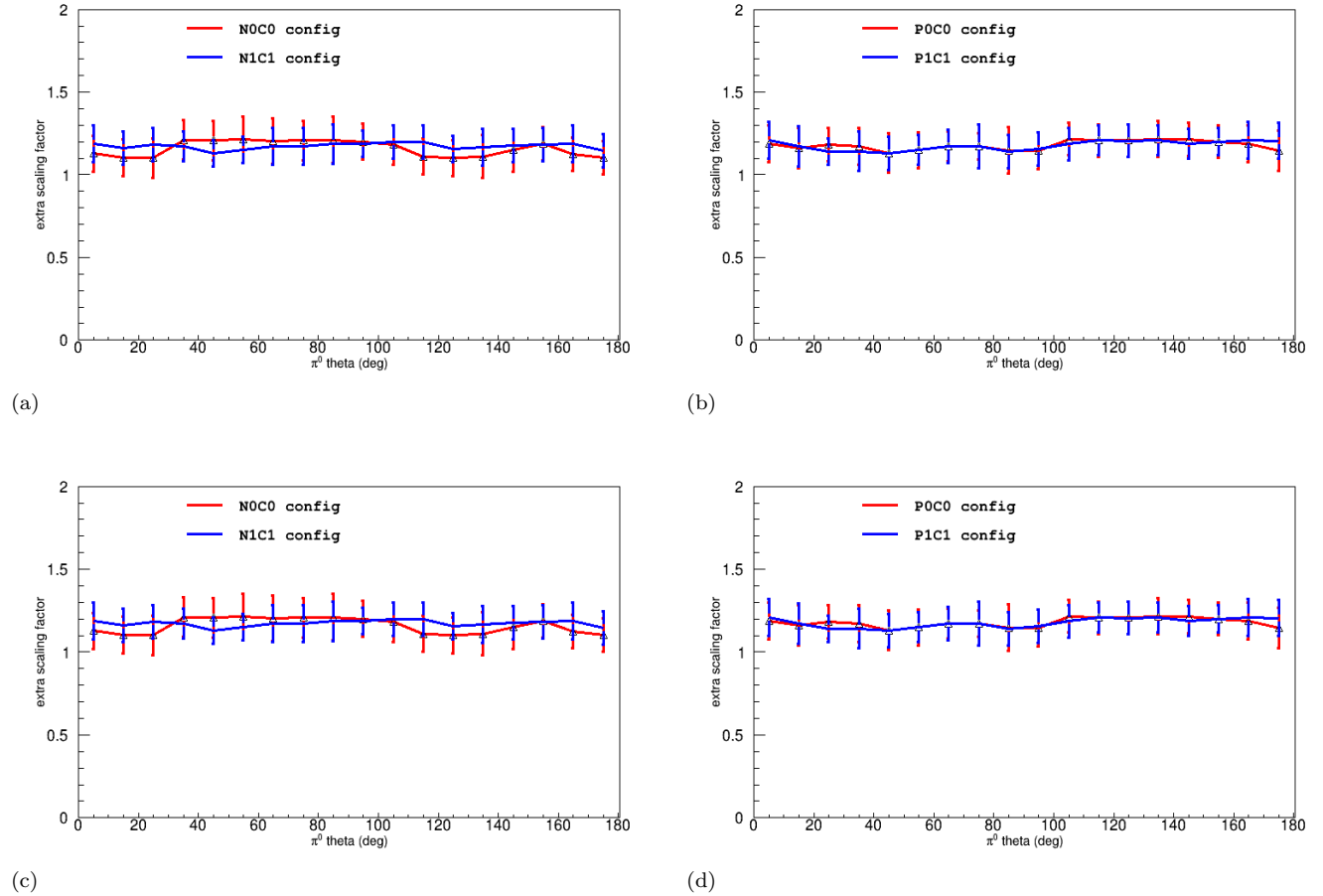

(a)

(b)

(c)

(d)

FIG. 40: Extra Carbon Scaling Factors. (a) and (b) show an extra carbon scaling factors for negatively and positively polarized target orientations from the 2014 beamtime, (c) and (d) from the 2015 beamtime.